ADVANCING EARTH AND SPACE SCIENCE

JGR Solid Earth

RESEARCH ARTICLE

10.1029/2021JB023809

Special Section:
Heterogeneity, anisotropy and scale-dependency: Keys to understand Earth composition, structure and behavior

Key Points:

- We present a wave propagation theory for partially saturated rocks with a fractal (self-similar) distribution of fluid patches
- We analyzed the effects of wave-induced local fluid flow on seismic attributes due to multi-scale fluid heterogeneities
- We estimated variations of the fluid distribution characteristics in partially-saturated rock samples by tying the data to the low frequency measurements

Correspondence to:

J. Ba,
jingba@188.com

Citation:

Zhang, L., Ba, J., Carcione, J. M., & Wu, C. (2022). Seismic wave propagation in partially saturated rocks with a fractal distribution of fluid-patch size. *Journal of Geophysical Research: Solid Earth*, *127*, e2021JB023809. https://doi.org/10.1029/2021JB023809

Received 10 DEC 2021
Accepted 26 JAN 2022

Author Contributions:

Conceptualization: Lin Zhang, Jing Ba
Data curation: Lin Zhang, Jing Ba, Chunfang Wu
Formal analysis: Lin Zhang, Jing Ba, José M. Carcione
Funding acquisition: Jing Ba
Investigation: Lin Zhang, Jing Ba, José M. Carcione, Chunfang Wu
Methodology: Lin Zhang, Jing Ba, José M. Carcione, Chunfang Wu
Project Administration: Jing Ba
Resources: Jing Ba
Software: Lin Zhang, Chunfang Wu
Supervision: Jing Ba, José M. Carcione
Validation: Lin Zhang, Jing Ba, Chunfang Wu

Seismic Wave Propagation in Partially Saturated Rocks With a Fractal Distribution of Fluid-Patch Size

Lin Zhang[1,2], Jing Ba[1], José M. Carcione[3], and Chunfang Wu[1]

[1]School of Earth Sciences and Engineering, Hohai University, Nanjing, China, [2]Earth, Atmospheric, and Planetary Sciences Department, Purdue University, West Lafayette, IN, USA, [3]National Institute of Oceanography and Applied Geophysics – OGS, Trieste, Italy

Abstract Laboratory experiments on partially saturated rocks show that seismic attenuation can be significant. The main mechanism, wave-induced local fluid flow (WILFF), is affected by the spatial fluid distribution, especially in conditions of patchy saturation at different spatial scales. We propose a theory to obtain the seismic properties of partially saturated rocks based on fractal (self-similar) patches, leading to an effective frequency-dependent fluid modulus. The model combines the differential effective medium and Biot-Rayleigh theories, where the patches are inclusions incrementally added, such that the effective fluid calculated in the current addition serves as host fluid in the next one. The analysis shows that adding identical inclusions in one or several steps produces nearly the same results, but the seismic properties depend on the scale range (radius) of the inclusions, fractal dimension D_f of the self-similar distribution, parameter θ of the exponential distribution, mean radius r_0 and variance σ_r^2 of the Gaussian distribution. Forced-oscillation experiments were performed on a limestone sample under partial water-saturation conditions at seismic frequencies (2–500 Hz), to obtain the velocity dispersion and extensional attenuation. The proposed theory provided a reasonable description of these experimental data as well as other published measurements on tight carbonate and Berea sandstone.

Plain Language Summary Seismic wave velocity dispersion and attenuation in partially saturated rock are affected by the size of the fluid patches, and their fractal dimension. To study this phenomenon, we have developed a wave propagation theory, in which the final partially saturated material is incrementally constructed by adding inclusions in size order into a homogenous frame saturated by a host fluid. We analyze the effects of wave-induced local fluid flow due to the multi-scale fluid heterogeneities on wave attributes. The broadband wave anelasticity predicted by the model is strongly affected by the scale range of the heterogeneities and their fractal dimension. The theory was compared with experimental data measured on different rock specimens and the fluid distribution characteristics at different saturations were estimated.

1. Introduction

Understanding how seismic-wave velocity dispersion and attenuation are affected by fluid saturation, properties and spatial distribution is important in several fields, such as geophysical prospecting and environmental sciences (e.g., Ciz et al., 2006; Kobayashi & Mavko, 2016; Lebedev et al., 2013; Lumley, 2001; Monachesi et al., 2020; Murphy et al., 1986; Solazzi et al., 2017). In particular, wave-induced local fluid flow (WILFF) is considered the main cause of the attenuation in partially saturated rocks, and occurs at different spatial scales (e.g., Müller et al., 2010).

When a seismic wave propagates through a partially saturated rock, it creates dissimilar fluid pressures in regions saturated by different fluids, inducing fluid flow and energy loss. At low frequencies, the characteristic patch size of fluid is much smaller than the diffusion length and the fluid pressure has enough time to equilibrate. Consequently, we consider that the effective fluid properties can be obtained with the Reuss equation and that the Gassmann equation yields the bulk modulus of the rock (Gassmann, 1951; Reuss, 1929). Conversely, at high frequencies when the characteristic patch size of fluid is much larger than the diffusion length, there is not enough time for pressure equilibration and the rock is unrelaxed with a higher bulk modulus. If the bulk modulus of each fluid patch is obtained with the Gassmann equation, the effective bulk modulus of the rock can be estimated with Hill's theorem (Hill, 1963). The two limits are the lower and upper bounds of the modulus of a partially saturated rock, known as Gassmann-Wood (GW) and Gassmann-Hill (GH) bounds, respectively.

Writing – original draft: Lin Zhang, Jing Ba, José M. Carcione
Writing – review & editing: Lin Zhang, Jing Ba, José M. Carcione, Chunfang Wu

To describe the behavior at intermediate frequencies, several models have been developed (Dutta & Seriff, 1979; Endres & Knight, 1991; Johnson, 2001; Mavko & Nolen-Hoeksema, 1994; Mavko & Nur, 1979; Papageorgiou & Chapman, 2017; Wang et al., 2021; White, 1975; White et al., 1975; Xiong et al., 2021), including numerical simulations (Carcione et al., 2003, 2011; Helle et al., 2003; Masson & Pride, 2007; Picotti et al., 2007; Quintal et al., 2011; Santos & Carcione, 2015; Santos et al., 2011; Wenzlau et al., 2010). White (1975) considered spherical gas pockets embedded in a water-saturated host rock. Using another approach based on a double-porosity model, Pride et al. (2004) and Ba et al. (2012) modeled the frequency-dependent seismic response caused by WILFF at the mesoscopic scale. Recently, Papageorgiou and Chapman (2015) considered a microstructural approach to model flow at the microscale (squirt flow).

All the aforementioned models rely on the assumption that the fluid patches have the same fixed size, and, consequently, cannot fully characterize the WILFF effect on wave propagation at different scales (Masson & Pride, 2011). To solve this problem, some theories considered a continuous random medium with exponential or Gaussian size distributions of the fluid patches (Müller & Gurevich, 2004; Toms et al., 2006, 2007; Toms-Stewart et al., 2009). Kobayashi and Mavko (2016) extended the work by Toms et al. (2007) and Toms-Stewart et al. (2009) to calculate the P-wave modulus dispersion of very strongly fluctuating media and compared their theoretical results to the laboratory measurements reported by Cadoret et al. (1995, 1998), where the actual fluid distribution was inferred from X-Ray CT scan images. It has been previously shown that a fractal model can usually be employed to describe the fluid-size distribution (Feder, 1988). Müller et al. (2008) also considered fractality and indeed found that the results varied between the GW and GH bounds depending on the fractal dimension, but the effect of WILFF at the microscopic scale was neglected. Le Ravalec et al. (1996) computed the effective elastic moduli in a partially saturated rock, in which both microscopic and mesoscopic fluid flows were present.

Many studies, especially experimental ones, show that the WILFF effect occurs at different scales (e.g., Agofack et al., 2018; Ba et al., 2019; Chapman et al., 2018; Li, Zhao, et al., 2020; Ma et al., 2018; Mikhaltsevitch et al., 2016; Murphy, 1982, 1984; Szewczyk et al., 2018; Tisato et al., 2021; Zhao et al., 2019). In particular, Adam et al. (2009) measured the elastic properties and attenuation of carbonate samples with different porosity and permeability at seismic and ultrasonic frequencies. Tisato and Quintal (2013) performed similar measurements on Berea sandstone from 1 to 100 Hz, and numerically solved Biot's consolidation equations to model fluid pressure diffusion. Li, Wang, et al. (2020) measured velocity dispersion on patchy saturated tight sandstone and carbonate samples at seismic frequencies, and concluded that it was likely caused by combined microscopic (squirt) and mesoscopic wave-induced fluid flow. Chapman et al. (2021) visualized the fluid distribution using medical X-ray computed tomography and measured the attenuation and modulus dispersion between 0.1 Hz and 1 kHz using the forced oscillation method. Moreover, they performed numerical simulations of fluid pressure diffusion, using the CO_2 saturation distribution derived from the X-ray CT scans as a direct input. While most of the models considered fabric heterogeneities (Ba et al., 2017; Sun & Gurevich, 2020; Zhang et al., 2019), less attention was paid to multi-scale fluid heterogeneities. Recently, Zhang et al. (2020, 2021) developed an infinituple-porosity model for a fluid-saturated rock to analyze the effects of fabric heterogeneities at multiple scales based on the differential effective medium theory.

In this work, a theoretical model (IPMPS) for describing wave anelasticity in rocks with fractal fluid patches is presented, based on the differential effective medium and Biot-Rayleigh theories. First, we derive the wave-propagation equations from the strain energy, kinetic energy and dissipation function (Section 2). We show how different self-similar fluid distributions affect the wave properties (Section 3). Then, we compare the model results with laboratory measurements performed with the forced oscillation method (Section 4). Finally, conclusions and recommendations are given in Section 5.

2. Model for Partially Saturated Rocks

2.1. Wave-Propagation Equations

In partially saturated rocks, the fluid patches have different shapes, sizes, and properties, such that the fluid distribution can be fractal (see Figure 1). In this study, we assume that there are two distinct, immiscible fluids, namely, a relatively incompressible one (e.g., a liquid such as water) and a very compressible one (e.g., gas). The first occupies a continuous, fully connected volume of rock (the host) surrounding a dilute concentration of spherical

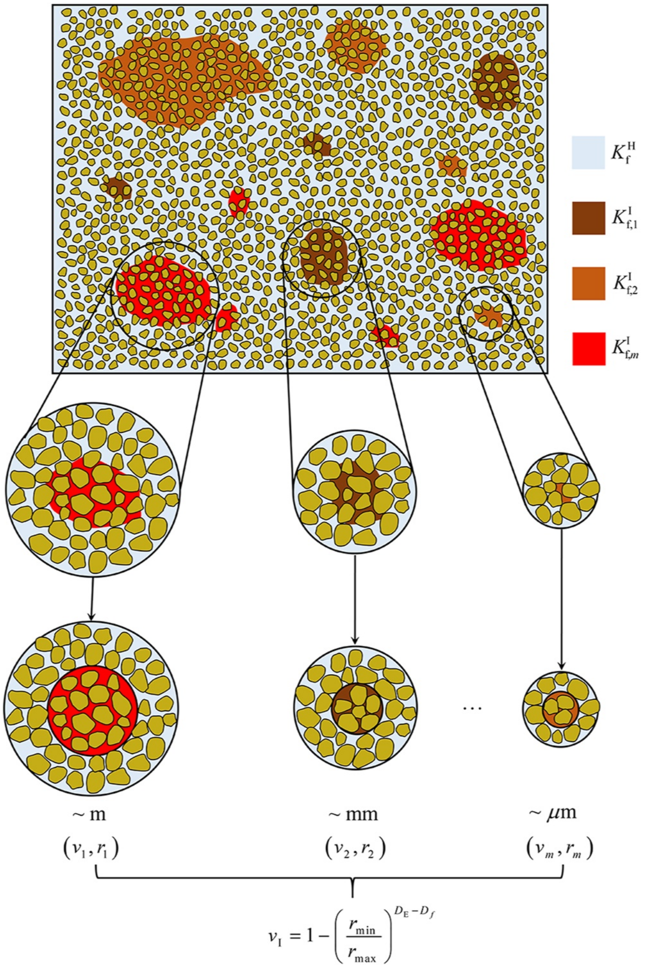

Figure 1. Fluid distribution in a homogenous frame, where K_f^H and $K_{f,m}^I$ are the bulk moduli of the host and inclusion fluids, respectively, v_m is the volume fraction of the m-th phase, r_{min} and r_{max} are the minimum and maximum inclusion radii, respectively, D_E is the Euclidean dimension, and D_f $(2 < D_f < 3)$ is the fractal dimension of the inclusion.

gas-saturated patches (the inclusions). The capillary pressure and the wetting properties of the two fluids are not considered in this model.

Similar to the differential effective medium theory for a solid composite (e.g., Berryman, 1992), a mathematical model of the partially saturated rock is proposed, that is, the inclusion phase is divided into infinite components (additions) that are incrementally incorporated into a homogeneous skeleton saturated by the host fluid, whereby each addition consists of a set of inclusions with the same radius. The inclusions from different additions have the same fluid type (bulk modulus K_f^I, density ρ_f^I and viscosity η_f^I), but different radii, which take m discrete values $r_1 > r_2 > \cdots > r_m$ according to a probability distribution such that the volume fraction is $\upsilon_I = 1 - (r_m/r_1)^{D_E - D_f}$, where $D_E = 3$ denotes the Euclidean dimension and D_f $(2 < D_f < 3)$ is the fractal dimension of the inclusion. Since the frame porosity ϕ_0 is assumed spatially constant (homogeneous solid frame), the volume fractions of the host (υ_H) and inclusions (υ_I) are equal to the liquid and gas saturations (S_H) and (S_I), respectively.

The starting point of our procedure is to consider a medium fully saturated with the host liquid, such that the initial host liquid saturation $S_{H,0}$ is equal to 1 and the inclusion gas saturation $S_{I,0} = 0$. In the first addition, the inclusions with radius r_1 and saturation S_1 are added and the gas and liquid saturations become $S_{I,1} = S_{I,0} + S_1$ and $S_{H,1} = S_{H,0} - S_1$, respectively, and the partial porosities corresponding to each fluid phases are $\phi_{I,1} = \phi_0 S_{I,1}$ and $\phi_{H,1} = \phi_0 S_{H,1}$. At the m-th iteration we have $S_{I,m} = S_{I,m\text{-}1} + S_m$ and $S_{H,m} = S_{H,m\text{-}1} - S_m$, where S_m is the saturation of the gas saturating the inclusions with radius r_m considered as a separate fluid phase. The partial porosities are $\phi_{I,m} = \phi_0 S_{I,m}$ and $\phi_{H,m} = \phi_0 S_{H,m}$. In each iteration, $S_0\,(S_{H,0}) + S_1 + \cdots + S_m = 1$ and the pore pressure remains constant.

For any addition, the partially saturated medium can be described as a double-porosity material, with $\phi_{I,m} = \phi_0 S_{I,m}$ and $\phi_{H,m} = \phi_0 S_{H,m}$ the partial porosities of the gas and liquid phases. The notations can be simplified by removing the subscript m, which refers to the m^{th} addition ($S_{H,m}$ will therefore be simply denoted by S and $\phi_{H,m} = \phi_0 S$). According to the differential effective medium theory, the two-phase material is constructed in steps by replacing infinitesimal volumes of host by equal volumes inclusions. Here, the increment in gas saturation of an addition is generally much smaller than the liquid saturation. Thus, $S_{I,m}$ can be considered an infinitesimal quantity and denoted $\mathrm{d}S$ and $\phi_{I,m} = \phi_0 \mathrm{d}S$. Finally, the equivalent response of such a medium can be obtained with the double-porosity Biot-Rayleigh theory (Ba et al., 2012), which describes the response of a homogeneous medium containing an effective fluid (i.e., the new host fluid in the next addition). On the basis of Ba et al. (2012), the strain energy is

$$\begin{aligned} 2W = &\left(\tilde{A} + 2\tilde{N}\right) I_1^2 - 4\tilde{N} I_2 + 2\tilde{Q}_H I_1 \left(\xi_H + \zeta\phi_0 \mathrm{d}S\right) + \tilde{R}_H\left(\xi_H + \zeta\phi_0 \mathrm{d}S\right)^2 \\ &+ 2\tilde{Q}_I I_1 \left(\xi_I - \phi_0 S\zeta\right) + \tilde{R}_I\left(\xi_I - \phi_0 S\zeta\right)^2 \end{aligned} \tag{1}$$

where I_1 and I_2 are the first and second strain invariants, and ξ_H and ξ_I are the fluid strains in the two pore phases saturated by the host and inclusion fluids, respectively. The scalar ζ denotes the fluid strain increment between the two pore phases. The stiffness coefficients are

$$\tilde{A} = (1 - \phi_0(S + \mathrm{d}S))\, K_s - \frac{2}{3}\tilde{N} - \tilde{Q}_H \frac{K_s}{K_f^H} - \tilde{Q}_I \frac{K_s}{K_f^I} \tag{2a}$$

$$\tilde{N} = G_b \tag{2b}$$

$$\tilde{Q}_{\mathrm{H}} = \frac{\phi_0 S \left(1 - \phi_0(S + \mathrm{d}S) - K_b/K_{\mathrm{s}}\right) K_{\mathrm{s}}}{1 - \phi_0(S + \mathrm{d}S) - K_b/K_{\mathrm{s}} + K_{\mathrm{s}}/K_{\mathrm{f}}^{\mathrm{H}} \phi_0(S + \mathrm{d}S)} \tag{2c}$$

$$\tilde{Q}_{\mathrm{I}} = \frac{\phi_0 \mathrm{d}S \left(1 - \phi_0(S + \mathrm{d}S) - K_b/K_{\mathrm{s}}\right) K_{\mathrm{s}}}{1 - \phi_0(S + \mathrm{d}S) - K_b/K_{\mathrm{s}} + K_{\mathrm{s}}/K_{\mathrm{f}}^{\mathrm{I}} \phi_0(S + \mathrm{d}S)} \tag{2d}$$

$$\tilde{R}_{\mathrm{H}} = \frac{\phi_0^2 S(S + \mathrm{d}S) K_{\mathrm{s}}}{1 - \phi_0(S + \mathrm{d}S) - K_b/K_{\mathrm{s}} + K_{\mathrm{s}}/K_{\mathrm{f}}^{\mathrm{H}} \phi_0(S + \mathrm{d}S)} \tag{2e}$$

$$\tilde{R}_{\mathrm{I}} = \frac{\phi_0^2 (S + \mathrm{d}S) K_{\mathrm{s}} \mathrm{d}S}{1 - \phi_0(S + \mathrm{d}S) - K_b/K_{\mathrm{s}} + K_{\mathrm{s}}/K_{\mathrm{f}}^{\mathrm{I}} \phi_0(S + \mathrm{d}S)} \tag{2f}$$

where K_{s} is the grain bulk modulus, K_b and G_b are the dry bulk and shear moduli of porous skeleton, respectively.

The kinetic energy is (Ba et al., 2012)

$$2T = \tilde{\rho}_{00} \sum_i \dot{u}_i^2 + 2\tilde{\rho}_{01} \sum_i \dot{u}_i \dot{U}_{i,\mathrm{H}} + 2\tilde{\rho}_{02} \sum_i \dot{u}_i \dot{U}_{i,\mathrm{I}} + \tilde{\rho}_{11} \sum_i \dot{U}_{i,\mathrm{H}}^2 + \tilde{\rho}_{22} \sum_i \dot{U}_{i,\mathrm{I}}^2 + 2T_{\mathrm{LFF}} \tag{3}$$

where $\mathbf{u} = [u_1, u_2, u_3]$, $\mathbf{U}_{\mathrm{H}} = \left[U_{1,\mathrm{H}}, U_{2,\mathrm{H}}, U_{3,\mathrm{H}}\right]$, and $\mathbf{U}_{\mathrm{I}} = \left[U_{1,\mathrm{I}}, U_{2,\mathrm{I}}, U_{3,\mathrm{I}}\right]$ are the solid displacement, and the fluid displacements of the two pore phases, respectively. T_{LFF} is the kinetic energy induced by the WILFF, that is,

$$T_{\mathrm{LFF}} = \frac{1}{6} \phi_0^3 S^2 \mathrm{d}S \rho_{\mathrm{f}}^{\mathrm{H}} r^2 \dot{\zeta}^2 \tag{4}$$

where $\rho_{\mathrm{f}}^{\mathrm{H}}$ is the density of the host fluid, and r is the inclusion radius.

The density coefficients are

$$\tilde{\rho}_{00} = \left(1 - \phi_0(S + \mathrm{d}S)\right) \rho_{\mathrm{s}} - \tilde{\rho}_{01} - \tilde{\rho}_{02} \tag{5a}$$

$$\tilde{\rho}_{01} = \phi_0 S \rho_{\mathrm{f}}^{\mathrm{H}} - \tilde{\rho}_{11} \tag{5b}$$

$$\tilde{\rho}_{02} = \rho_{\mathrm{f}}^{\mathrm{I}} \phi_0 \mathrm{d}S - \tilde{\rho}_{22} \tag{5c}$$

$$\tilde{\rho}_{11} = \alpha \phi_0 S \rho_{\mathrm{f}}^{\mathrm{H}} \tag{5d}$$

$$\tilde{\rho}_{22} = \alpha \rho_{\mathrm{f}}^{\mathrm{I}} \phi_0 \mathrm{d}S \tag{5e}$$

where ρ_{s} is the grain density, and α is the tortuosity of the skeleton, which can be determined as (Berryman, 1979)

$$\alpha = \frac{1}{2}\left(1 + \frac{1}{\phi_0}\right) \tag{6}$$

The dissipation function is

$$2D = \tilde{b}_1 \left(\dot{\mathbf{u}} - \dot{\mathbf{U}}_{\mathrm{H}}\right)\left(\dot{\mathbf{u}} - \dot{\mathbf{U}}_{\mathrm{H}}\right) + \tilde{b}_2 \left(\dot{\mathbf{u}} - \dot{\mathbf{U}}_{\mathrm{I}}\right)\left(\dot{\mathbf{u}} - \dot{\mathbf{U}}_{\mathrm{I}}\right) + 2D_{\mathrm{LFF}} \tag{7}$$

where

$$D_{\mathrm{LFF}} = \frac{1}{6} \frac{\eta_{\mathrm{f}}^{\mathrm{H}}}{\kappa_{\mathrm{H}}} \phi_0^4 S^2 \mathrm{d}S r^2 \dot{\zeta}^2 \tag{8}$$

is the dissipation energy induced by the WILFF, $\eta_{\mathrm{f}}^{\mathrm{H}}$ is the viscosity of the host fluid, κ_{H} is the permeability of the skeleton, and

$$\tilde{b}_1 = \phi_0^2 S \frac{\eta_{\mathrm{f}}^{\mathrm{H}}}{\kappa_{\mathrm{H}}} \tag{9a}$$

$$\tilde{b}_2 = \phi_0^2 \mathrm{d}S \frac{\eta_\mathrm{f}^\mathrm{I}}{\kappa_\mathrm{H}} \tag{9b}$$

Based on Hamilton's principle and the Lagrangian $L = T - W$, the governing equations of wave propagation are

$$\begin{aligned}&\tilde{N}\nabla^2\mathbf{u} + \left(\tilde{A}+\tilde{N}\right)\nabla e + \tilde{Q}_\mathrm{H}\nabla\left(\xi_\mathrm{H} + \zeta\phi_0\mathrm{d}S\right) + \tilde{Q}_\mathrm{I}\nabla\left(\xi_\mathrm{I} - \phi_0 S\zeta\right)\\ &= \tilde{\rho}_{00}\ddot{\mathbf{u}} + \tilde{\rho}_{01}\ddot{\mathbf{U}}_\mathrm{H} + \tilde{\rho}_{02}\ddot{\mathbf{U}}_\mathrm{I} + \tilde{b}_1\left(\dot{\mathbf{u}} - \dot{\mathbf{U}}_\mathrm{H}\right) + \tilde{b}_2\left(\dot{\mathbf{u}} - \dot{\mathbf{U}}_\mathrm{I}\right)\end{aligned} \tag{10a}$$

$$\tilde{Q}_\mathrm{H}\nabla e + \tilde{R}_\mathrm{H}\nabla\left(\xi_\mathrm{H} + \zeta\phi_0\mathrm{d}S\right) = \tilde{\rho}_{01}\ddot{\mathbf{u}} + \tilde{\rho}_{11}\ddot{\mathbf{U}}_\mathrm{H} - \tilde{b}_1\left(\dot{\mathbf{u}} - \dot{\mathbf{U}}_\mathrm{H}\right) \tag{10b}$$

$$\tilde{Q}_\mathrm{I}\nabla e + \tilde{R}_\mathrm{I}\nabla\left(\xi_\mathrm{I} - \phi_0 S\zeta\right) = \tilde{\rho}_{02}\ddot{\mathbf{u}} + \tilde{\rho}_{22}\ddot{\mathbf{U}}_\mathrm{I} - \tilde{b}_2\left(\dot{\mathbf{u}} - \dot{\mathbf{U}}_\mathrm{I}\right) \tag{10c}$$

$$\left(\tilde{Q}_\mathrm{H}\nabla e + \tilde{R}_\mathrm{H}\nabla\left(\xi_\mathrm{H} + \zeta\phi_0\mathrm{d}S\right)\right)\mathrm{d}S - S\left(\tilde{Q}_\mathrm{I}\nabla e + \tilde{R}_\mathrm{I}\nabla\left(\xi_\mathrm{I} - \phi_0 S\zeta\right)\right) = \frac{1}{3}r^2\phi_0^3 S^2\mathrm{d}S\left(\frac{\rho_\mathrm{f}^\mathrm{H}}{\phi_0}\ddot{\zeta} + \frac{\eta_\mathrm{f}^\mathrm{H}}{\kappa_\mathrm{H}}\dot{\zeta}\right) \tag{10d}$$

where e is the solid divergence field. The stiffness, density and dissipation coefficients in Equations 2, 5, and 9 are also functions of S and $\mathrm{d}S$. Hence, there are high-order terms of $\mathrm{d}S$ in Equation 10. Let us define

$$B_1 = \left(1 - \phi_0 S - K_b/K_\mathrm{s} + K_\mathrm{s}/K_\mathrm{f}^\mathrm{H}\phi_0 S\right) + \left(-1 + K_\mathrm{s}/K_\mathrm{f}^\mathrm{H}\right)\phi_0\mathrm{d}S \tag{11a}$$

$$B_2 = \left(1 - \phi_0 S - K_b/K_\mathrm{s} + K_\mathrm{s}/K_\mathrm{f}^\mathrm{I}\phi_0 S\right) + \left(-1 + K_\mathrm{s}/K_\mathrm{f}^\mathrm{I}\right)\phi_0\mathrm{d}S \tag{11b}$$

and multiply Equations 10a and 10d by B_1B_2, Equation 10b by B_1, and Equation 10c by B_2. Neglecting the high-order terms in $\mathrm{d}S$, we obtain

$$\begin{aligned}&(N + NZ\phi_0\mathrm{d}S)\nabla^2\mathbf{u} + (A+N)\nabla e + (A_\mathrm{d} + NZ)\phi_0\mathrm{d}S\nabla e + Q_\mathrm{H}\phi_0 S\nabla\left(\xi_\mathrm{H} + \zeta\phi_0\mathrm{d}S\right)\\ &+ R_\mathrm{H}\left(\frac{Q_\mathrm{I}}{K_\mathrm{f}^\mathrm{I}} - \frac{Q_\mathrm{I}}{K_\mathrm{s}} - 1\right)\phi_0\mathrm{d}S\nabla\xi_\mathrm{H} + Q_\mathrm{I}\phi_0\mathrm{d}S\nabla\left(\xi_\mathrm{I} - \phi_0 S\zeta\right)\\ &= \rho_{00}\ddot{\mathbf{u}} + (\rho_{00}Z - \rho_\mathrm{s} - \rho_{02})\phi_0\mathrm{d}S\ddot{\mathbf{u}} + \rho_{01}\phi_0 S\ddot{\mathbf{U}}_\mathrm{H} + \rho_{01}\phi_0^2 ZS\mathrm{d}S\ddot{\mathbf{U}}_\mathrm{H} + \rho_{02}\phi_0\mathrm{d}S\ddot{\mathbf{U}}_\mathrm{I}\\ &+ \frac{\phi_0^2 S\eta_\mathrm{f}^\mathrm{H}}{\kappa_\mathrm{H}}\left(\dot{\mathbf{u}} - \dot{\mathbf{U}}_\mathrm{H}\right) + \frac{\phi_0^3 S\eta_\mathrm{f}^\mathrm{H}}{\kappa_\mathrm{H}}Z\mathrm{d}S\left(\dot{\mathbf{u}} - \dot{\mathbf{U}}_\mathrm{H}\right) + \frac{\phi_0^2\eta_\mathrm{f}^\mathrm{I}\mathrm{d}S}{\kappa_\mathrm{H}}\left(\dot{\mathbf{u}} - \dot{\mathbf{U}}_\mathrm{I}\right)\end{aligned} \tag{12a}$$

$$\begin{aligned}&Q_\mathrm{H}\nabla e + R_\mathrm{H}\nabla\left(\xi_\mathrm{H} + \zeta\phi_0\mathrm{d}S\right) + \frac{R_\mathrm{H}}{\phi}\left(\nabla\xi_\mathrm{H} - \nabla e\right)\phi_0\mathrm{d}S\\ &= \left(1 + \frac{R_\mathrm{H}}{S}\left(\frac{1}{K_\mathrm{f}^\mathrm{H}} - \frac{1}{K_\mathrm{s}}\right)\mathrm{d}S\right)\left(\rho_{01}\ddot{\mathbf{u}} + \rho_{11}\ddot{\mathbf{U}}_\mathrm{H} - \frac{\phi_0\eta_\mathrm{f}^\mathrm{H}}{\kappa_\mathrm{H}}\left(\dot{\mathbf{u}} - \dot{\mathbf{U}}_\mathrm{H}\right)\right)\end{aligned} \tag{12b}$$

$$Q_\mathrm{I}\nabla e + R_\mathrm{I}\nabla\left(\xi_\mathrm{I} - \phi_0 S\zeta\right) = \rho_{02}\ddot{\mathbf{u}} + \rho_{22}\ddot{\mathbf{U}}_\mathrm{I} - \frac{\phi_0\eta_\mathrm{f}^\mathrm{I}}{\kappa_\mathrm{H}}\left(\dot{\mathbf{u}} - \dot{\mathbf{U}}_\mathrm{I}\right) \tag{12c}$$

$$\left(Q_\mathrm{H}e + R_\mathrm{H}\left(\xi_\mathrm{H} + \zeta\phi_0\mathrm{d}S\right)\right) - \left(Q_\mathrm{I}e + R_\mathrm{I}\left(\xi_\mathrm{I} - \phi_0 S\zeta\right)\right) = \frac{1}{3}r^2\phi_0^2 S\left(\frac{\rho_\mathrm{f}^\mathrm{H}}{\phi_0}\ddot{\zeta} + \frac{\eta_\mathrm{f}^\mathrm{H}}{\kappa_\mathrm{H}}\dot{\zeta}\right) \tag{12d}$$

where

$$A = (1 - \phi_0 S)K_\mathrm{s} - \frac{2}{3}N - K_\mathrm{s}/K_\mathrm{f}^\mathrm{H}Q_\mathrm{H}\phi_0 S \tag{13a}$$

$$A_\mathrm{d} = (1 - \phi_0 S)K_\mathrm{s}Z - \frac{2}{3}NZ - Q_\mathrm{I}R_\mathrm{H}\left(K_\mathrm{s}/\left(K_\mathrm{f}^\mathrm{H}K_\mathrm{f}^\mathrm{I}\right) - 1/K_\mathrm{f}^\mathrm{H}\right) - Q_\mathrm{I}K_\mathrm{s}/K_\mathrm{f}^\mathrm{I} + R_\mathrm{H}K_\mathrm{s}/K_\mathrm{f}^\mathrm{H} - K_\mathrm{s} \tag{13b}$$

$$N = \tilde{N} \tag{13c}$$

$$Q_\mathrm{H} = \frac{K_\mathrm{s}\left(1 - \phi_0 S - K_b/K_\mathrm{s}\right)}{1 - \phi_0 S - K_b/K_\mathrm{s} + K_\mathrm{s}/K_\mathrm{f}^\mathrm{H}\phi_0 S} \tag{13d}$$

$$Q_{\rm I} = \frac{K_{\rm s}\left(1 - \phi_0 S - K_b/K_{\rm s}\right)}{1 - \phi_0 S - K_b/K_{\rm s} + K_{\rm s}/K_{\rm f}^{\rm I}\phi_0 S} \tag{13e}$$

$$R_{\rm H} = \frac{K_{\rm s}\phi_0 S}{1 - \phi_0 S - K_b/K_{\rm s} + K_{\rm s}/K_{\rm f}^{\rm H}\phi_0 S} \tag{13f}$$

$$R_{\rm I} = \frac{K_{\rm s}\phi_0 S}{1 - \phi_0 S - K_b/K_{\rm s} + K_{\rm s}/K_{\rm f}^{\rm I}\phi_0 S} \tag{13g}$$

$$Z = R_{\rm H}/\left(\phi_0 S\right)\left(1/K_{\rm f}^{\rm H} - 1/K_{\rm s}\right) + R_{\rm I}/\left(\phi_0 S\right)\left(1/K_{\rm f}^{\rm I} - 1/K_s\right) \tag{13h}$$

$$\rho_{00} = \left(1 - \phi_0 S\right)\rho_{\rm s} - \phi_0 S\rho_{01} \tag{13i}$$

$$\rho_{01} = (1 - \alpha)\rho_{\rm f}^{\rm H} \tag{13j}$$

$$\rho_{02} = (1 - \alpha)\rho_{\rm f}^{\rm I} \tag{13k}$$

$$\rho_{11} = \alpha\rho_{\rm f}^{\rm H} \tag{13l}$$

$$\rho_{22} = \alpha\rho_{\rm f}^{\rm I} \tag{13m}$$

We note that the stiffness and density coefficients in Equation 13 are dependent on S and first-order terms in dS appear in Equation 12.

The P- and S-wave complex wave numbers (k_P and k_S) are obtained with a plane-wave analysis of Equation 12 (see Equations B1–B4 in Ba et al. (2011)). Then, the complex bulk and shear moduli of the composite porous medium are

$$K_{\rm sat} = \left(\left(1 - \phi_0(S + {\rm d}S)\right)\rho_{\rm s} + \phi_0(S + {\rm d}S)\rho_{\rm f}\right)\left(\frac{\omega}{k_P}\right)^2 - \frac{4}{3}G_{\rm sat} \tag{14a}$$

$$G_{\rm sat} = \left(\left(1 - \phi_0(S + {\rm d}S)\right)\rho_{\rm s} + \phi_0(S + {\rm d}S)\rho_{\rm f}\right)\left(\frac{\omega}{k_S}\right)^2 \tag{14b}$$

where ω is the angular frequency, and $\rho_{\rm f}$ is the effective fluid density $\rho_{\rm f} = \rho_{\rm f}^{\rm H}S_{\rm H} + \rho_{\rm f}^{\rm I}S_{\rm I}$. According to the classic poroelasticity theory (Biot, 1956), in homogeneous porous media, there is a weak dispersion effect for both the P- and S-wave velocities (bulk and shear moduli) related to the relative displacements of the solid frame and pore fluid.

In summary, at the end of each addition, the equivalent homogeneous medium is considered a homogeneous porous medium saturated by an effective fluid with a complex bulk modulus. This bulk modulus can be obtained from Gassmann equations (Gassmann, 1951), and is used to define the bulk modulus of the host fluid in the next addition:

$$\frac{K_{\rm sat}}{K_{\rm s} - K_{\rm sat}} = \frac{K_b}{K_{\rm s} - K_b} + \frac{K_{\rm f}}{\phi_0(S + {\rm d}S)\left(K_{\rm s} - K_{\rm f}\right)} \tag{15}$$

By using Equations 12–15 in each addition and stopping the addition procedure when the desired fluid saturations are reached, we can incrementally construct the partially saturated rock and calculate the bulk modulus of the final effective fluid.

2.2. Infinituple-Porosity (IPMPS) Model

The size of the inclusions obeys a correlation function (Klimeš, 2002), with d$S = S'(r)dr$. The equations of the IPMPS model are

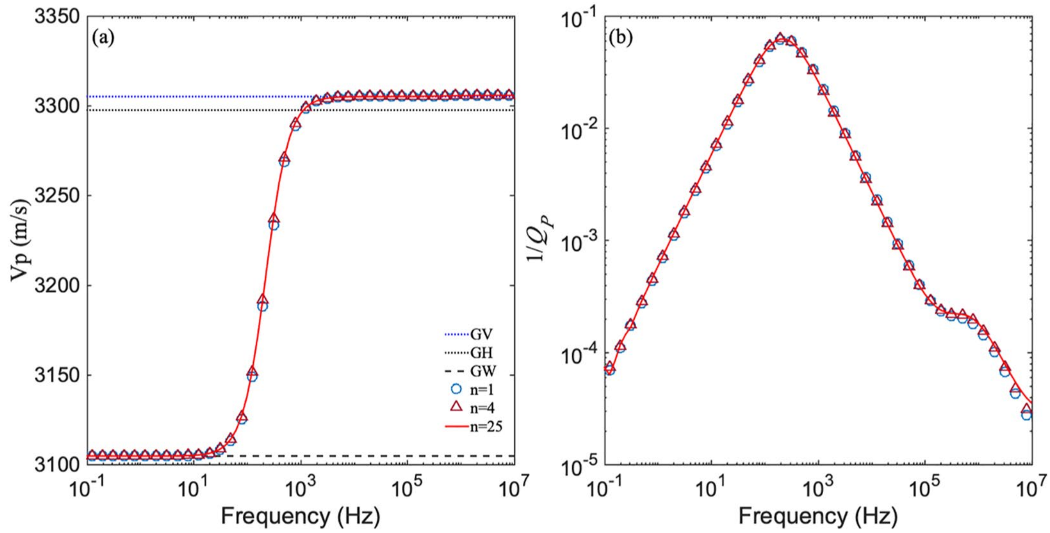

Figure 2. P-wave velocity (a) and attenuation (b) as a function of frequency for a partially saturated rock with $n = 1$, 4, and 25 additions, where 5% weakly compressible gas is the inclusion fluid. The limits of GW, GH, and GV are given.

$$\bar{N}\nabla^2\mathbf{u} + \left(\bar{A}+\bar{N}\right)\nabla e + \bar{Q}_{\mathrm{H}}\phi_0 S\nabla\left(\xi_{\mathrm{H}} + \int_0^\infty \zeta\phi_0 S'(r)dr\right) + \int_0^\infty \bar{Q}_{\mathrm{I}}\phi_0 S'(r)\nabla\left(\xi_{\mathrm{I}} - \phi_0 S\zeta\right)dr$$
$$= \bar{\rho}_{00}\ddot{\mathbf{u}} + \bar{\rho}_{01}\phi_0 S\ddot{\mathbf{U}}_{\mathrm{H}} + \int_0^\infty \bar{\rho}_{02}\phi_0 S'(r)\ddot{\mathbf{U}}_{\mathrm{I}}dr + \frac{\phi_0^2 S\eta_{\mathrm{f}}^{\mathrm{H}}}{\kappa_{\mathrm{H}}}\left(\dot{\mathbf{u}}-\dot{\mathbf{U}}_{\mathrm{H}}\right) + \eta_{\mathrm{f}}^{\mathrm{I}}\int_0^\infty \frac{\phi_0^2}{\kappa_{\mathrm{H}}}\left(\dot{\mathbf{u}}-\dot{\mathbf{U}}_{\mathrm{I}}\right)S'(r)dr \tag{16a}$$

$$\bar{Q}_{\mathrm{H}}\nabla e + \bar{R}_{\mathrm{H}}\nabla\left(\xi_{\mathrm{H}} + \int_0^\infty \phi_0 S'(r)\zeta dr\right) = \bar{\rho}_{01}\ddot{\mathbf{u}} + \bar{\rho}_{11}\ddot{\mathbf{U}}_{\mathrm{H}} - \frac{\phi_0\eta_{\mathrm{f}}^{\mathrm{H}}}{\kappa_{\mathrm{H}}}\left(\dot{\mathbf{u}}-\dot{\mathbf{U}}_{\mathrm{H}}\right) \tag{16b}$$

$$\bar{Q}_{\mathrm{I}}\nabla e + \bar{R}_{\mathrm{I}}\nabla\left(\xi_{\mathrm{I}} - \phi_0 S\zeta\right) = \bar{\rho}_{02}\ddot{\mathbf{u}} + \bar{\rho}_{22}\ddot{\mathbf{U}}_{\mathrm{I}} - \frac{\phi_0\eta_{\mathrm{f}}^{\mathrm{I}}}{\kappa_{\mathrm{H}}}\left(\dot{\mathbf{u}}-\dot{\mathbf{U}}_{\mathrm{I}}\right) \tag{16c}$$

$$\left(\bar{Q}_{\mathrm{H}}e + \bar{R}_{\mathrm{H}}\left(\xi_{\mathrm{H}} + \int_0^\infty \zeta\phi_0 S'(r)dr\right)\right) - \left(\bar{Q}_{\mathrm{I}}e + \bar{R}_{\mathrm{I}}\left(\xi_{\mathrm{I}} - \phi_0 S\zeta\right)\right) = \frac{1}{3}r^2\phi_0^2 S\left(\frac{\rho_{\mathrm{f}}}{\phi_0}\ddot{\zeta} + \frac{\eta_{\mathrm{f}}^{\mathrm{H}}}{\kappa_{\mathrm{H}}}\dot{\zeta}\right) \tag{16d}$$

where the stiffnesses $\bar{A}$, $\bar{N}$, $\bar{Q}_{\mathrm{H}}$, $\bar{Q}_{\mathrm{I}}$, $\bar{R}_{\mathrm{H}}$ and $\bar{R}_{\mathrm{I}}$, and the density coefficients $\bar{\rho}_{00}$, $\bar{\rho}_{01}$, $\bar{\rho}_{02}$, $\bar{\rho}_{11}$, and $\bar{\rho}_{22}$, are obtained on the basis of the discretization procedure of Section 2.1, where Equations 12–15 are used in each iteration and the final P- and S- wave numbers are obtained at the last iteration, to compute the wave velocity and attenuation.

3. Examples

3.1. Wave Propagation in a Double-Porosity Medium

Table 1
Rock and Pore-Fluid Properties

Rock		Fluids			52
K_b	7 GPa	K_{fw} (water)	2.25 Gpa	K_{fa} (air)	0.1 Mpa
G_b	9 GPa	ρ_{w}	990 kg/m^3	ρ_{a}	100 kg/m^3
K_{s}	35 GPa	η_{w}	0.001 Pa•s	η_{a}	0.00001 Pa•s
ρ_{s}	2,650 kg/m^3	K_{fg} (Gas)	0.1 GPa		
ϕ	0.15	ρ_{g}	100 kg/m^3		
κ	0.01 D	η_{g}	0.00003 Pa•s		

In order to illustrate the proposed model, we consider the P-wave velocity ($\mathrm{V_P}$) and attenuation (dissipation factor, $1/Q_P$) of a gas-water saturated rock, where 5% of a weakly compressible gas (inclusions) is added into a water-saturated host medium. When all the inclusions have the same radius ($r_0 = 5$ mm) and physical properties, they are added as one addition into the host. In this case, the IPMPS model reduces to a double-porosity model. Comparisons between the modeling results for $n = 1$, 4, 25 additions are given in Figure 2 and the rock and fluid properties are given in Table 1. The results are almost the same for the different additions, indicating that when the inclusions have the same size and properties, the P-wave velocity and attenuation is independent of the number of additions. At low frequencies, the P-wave velocity approaches the GW limit, while at high frequencies it is slightly higher than the GH limit and, in fact, approaches the Gassmann-Voigt (GV) limit. The effective bulk modulus (K_{GV}) is estimated from the Voigt equation by using the bulk modulus of each phase obtained with the Gassmann equation, that is,

$$\left(K_{\mathrm{GV}}+\frac{4}{3}G_b\right)=S_{\mathrm{w}}\left(K_{\mathrm{Gw}}+\frac{4}{3}G_b\right)+S_{\mathrm{g}}\left(K_{\mathrm{Gg}}+\frac{4}{3}G_b\right) \tag{17}$$

where K_{Gw} and K_{Gg} are the rock bulk moduli according to Gassmann equation for regions saturated with water and gas, respectively. S_{w} and S_{g} are the water and gas saturations, respectively. The GV limit indicates that the partially saturated rock is in an iso-strain state, which can be considered a reasonable upper bound of the proposed model.

In a second example, we perform the same analysis but with air as inclusion fluid, whose properties are given in Table 1. Figure 3 shows the results for $n = 1$, 4, 25 additions, where similar conclusions as those of Figure 2 are obtained, demonstrating that the model can handle cases with very dissimilar fluid compressibilities.

3.2. Wave Propagation With a Fractal Fluid-Size Distribution

In the following, we assume that the size of the inclusions can be described by a self-similar distribution (Figure 1), where their volume fractions are related to the inclusion scale as (Rieu & Perrier, 1998)

$$\upsilon_{\mathrm{I}}=1-(r_{\min}/r_{\max})^{D_{\mathrm{E}}-D_f} \tag{18}$$

Figure 4 shows the P-wave velocity and attenuation for varying fractal dimension and a distributed range of the inclusion radius. The properties are listed in Table 1. The results show that when the inclusion size ranges are the same (for black, red, blue and brown solid curves), the P-wave velocity decreases with increasing D_f, and the attenuation also shows a similar behavior in the frequency range 10^{-1}–$10^{4.8}$ Hz, whereas the attenuation increases with D_f in the range $10^{4.8}$–10^{7} Hz. At the same D_f (for blue dashed and solid curves), the P-wave velocity decreases with increasing scale range of the radius.

The P-wave velocity and attenuation as a function of S_{w} for $D_f = 2.78$ and different frequencies are shown in Figure 5, where the scale range is (0.1–100) mm. It is observed that for seismic frequencies (i.e., $f = 100$ Hz), the P-wave velocity decreases slightly as saturation increases from $S_{\mathrm{w}} = 0\%$ to 40%. This is because the effect of the effective density on the velocity is comparable or greater than that of the effective P-wave modulus. In contrast, the velocity increases drastically from $S_{\mathrm{w}} = 40\%$ to 100%. The corresponding attenuation peak is located at $S_{\mathrm{w}} = 90\%$. A similar behavior is observed at sonic frequencies (i.e., $f = 10^4$ Hz), where the velocity decreases with saturation increasing from $S_{\mathrm{w}} = 0\%$ to 20%, and increases with further saturation increase from $S_{\mathrm{w}} = 20\%$

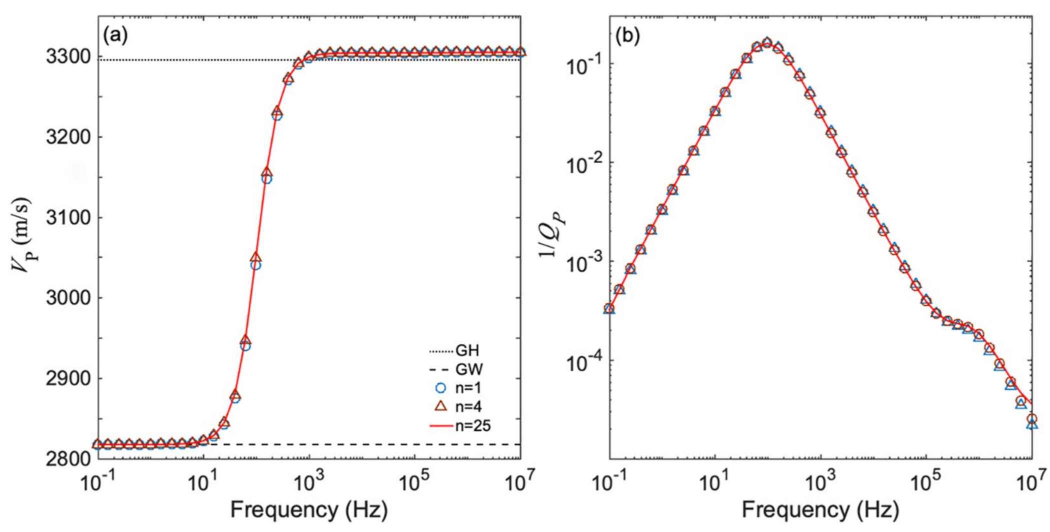

Figure 3. P-wave velocity (a) and attenuation (b) as a function of frequency for a partially saturated rock with $n = 1$, 4, and 25 additions, where 5% air is the inclusion fluid.

10.1029/2021JB023809

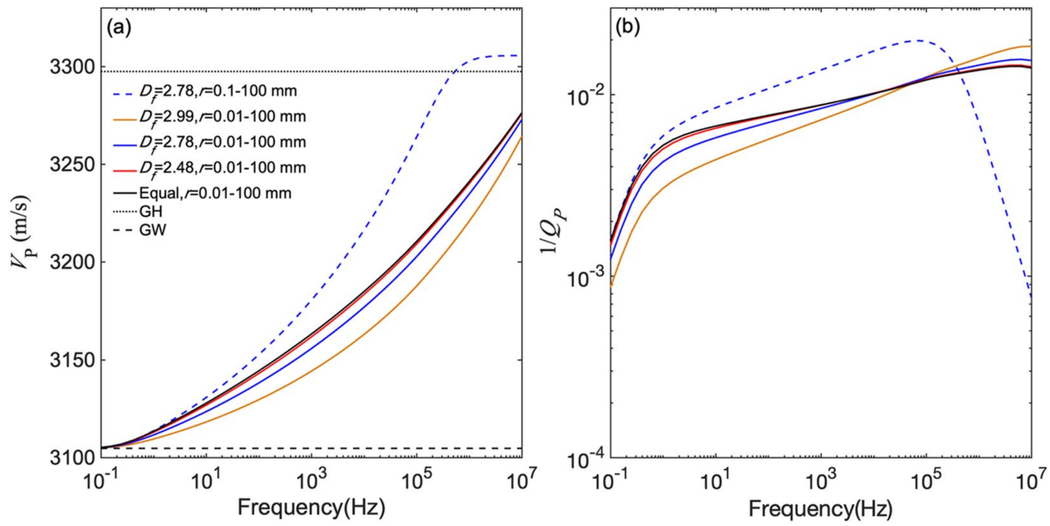

Figure 4. P-wave velocity (a) and attenuation (b) as a function of frequency for a partially saturated rock with varying D_f and a distributed range of inclusion fluid radii, where 5% weakly compressible gas is the inclusion fluid.

to 100%. The corresponding attenuation peak is located at $S_w = 85\%$. At ultrasonic frequencies (i.e., $f = 10^6$ Hz), the velocity increases as S_w increases, and the attenuation peak is located at $S_w = 47.5\%$. Then, the attenuation peak moves toward lower water saturations with increasing frequency. A similar behavior is observed in figure 6b of Solazzi et al. (2019).

3.3. Comparison Between Different Patch Distributions

The pore-fluid distribution can be described by the self-similar, exponential or Gaussian distributions (Helle et al., 2003; Müller et al., 2008; Toms et al., 2007). The examples for gas and water partial saturation are given in Figure 6 (the procedure for constructing the fluid distribution at given water saturations can be found in Helle et al. (2003)).

Next, we consider cases where the patch distribution is exponential and Gaussian, other than self-similar. The exponential distribution is defined by a parameter θ (i.e., $\upsilon_I = 1/\theta e^{-r/\theta}$), and the Gaussian distribution by the mean

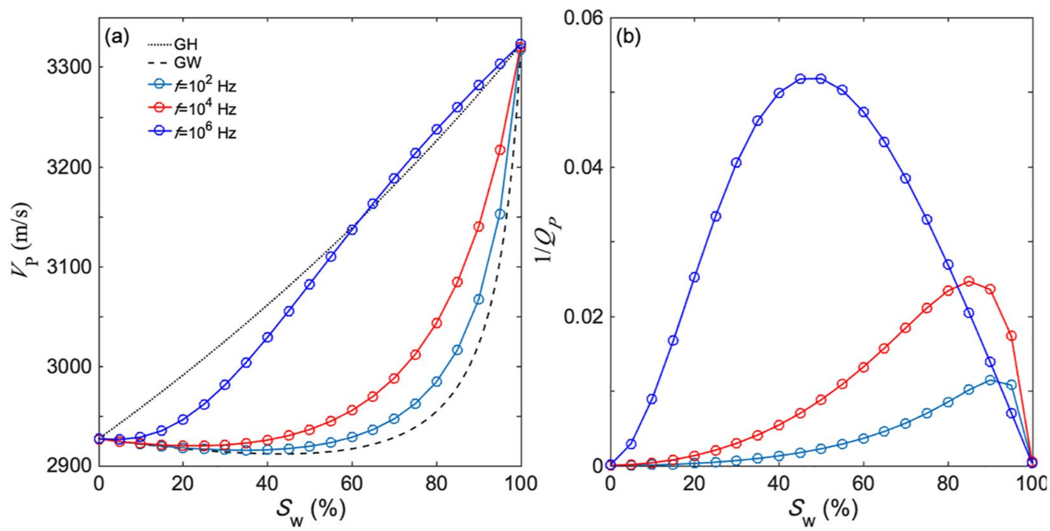

Figure 5. P-wave velocity (a) and attenuation (b) as a function of water saturation and different frequencies and $D_f = 2.78$, where weakly compressible gas is the inclusion fluid.

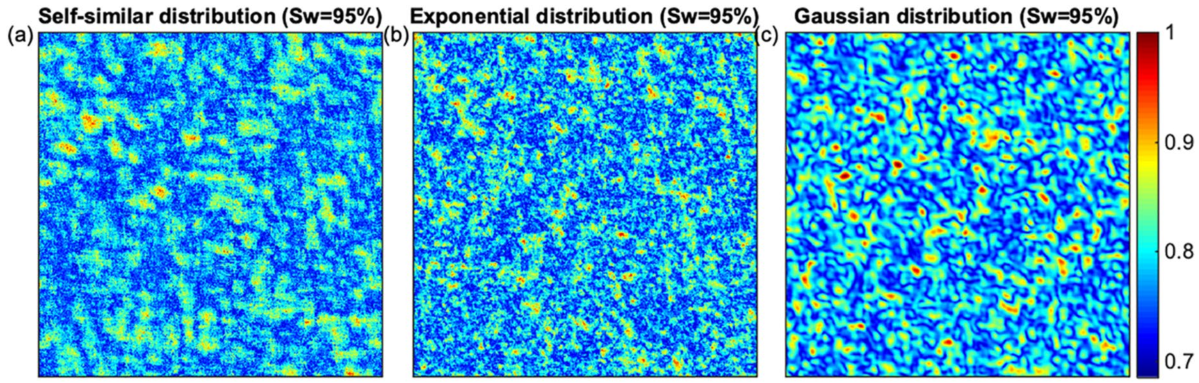

Figure 6. Examples of the self-similar (a), exponential (b), and Gaussian (c) distributions of the fluid for $S_w = 95\%$. The color bar indicates water saturation. Grid size is 0.1 mm. The correlation length is 1 mm and $D_f = 2.9$. The scale of the maps is 6×6 cm.

radius r_0 and variance σ_r^2 of the inclusions (i.e., $\upsilon_I = 1/\sqrt{2\pi\sigma_r^2}e^{-(r-r_0)^2/(2\sigma_r^2)}$). The results are shown in Figure 7, where we can see similar behaviors when $D_f = 2$, $\theta = 1$ and $r_0 = 1$ mm and $\sigma_r^2 = 1$ (red, brown, and blue dashed curves). This is because each added inclusion phase has nearly the same volume fraction and inclusion radius. The range of wave dispersion and attenuation of $D_f = 2.99$ is wider than that of $D_f < 2.99$ for the self-similar distribution (red dashed and solid curves). The range for $\theta = 1$ is wider than that of $\theta < 1$ for the exponential distribution (brown dashed and solid curves), and the range for $\sigma_r^2 = 1$ is wider than that of $\sigma_r^2 < 1$ for the Gaussian distribution (blue dashed and solid curves). These conclusions are consistent with the results observed for rock-fabric heterogeneity using the three distributions (see Figure 6 in Zhang et al., 2021).

4. Comparisons With Laboratory Measurements

4.1. Limestone

We performed experiments on a limestone sample, 38.14 mm in diameter and 49.87 mm in length, from the Metajan area located on the right bank block of the Amu Darya River. The rock has a porosity of 0.1248 and a permeability of 0.1 mD, and is composed of calcite (>95%), with small amounts of clay minerals (<5%). According to the thin section analysis of other samples from the same formation (Yu et al., 2014), the limestone samples do not have a lot of microporosity, although they are fairly heterogeneous.

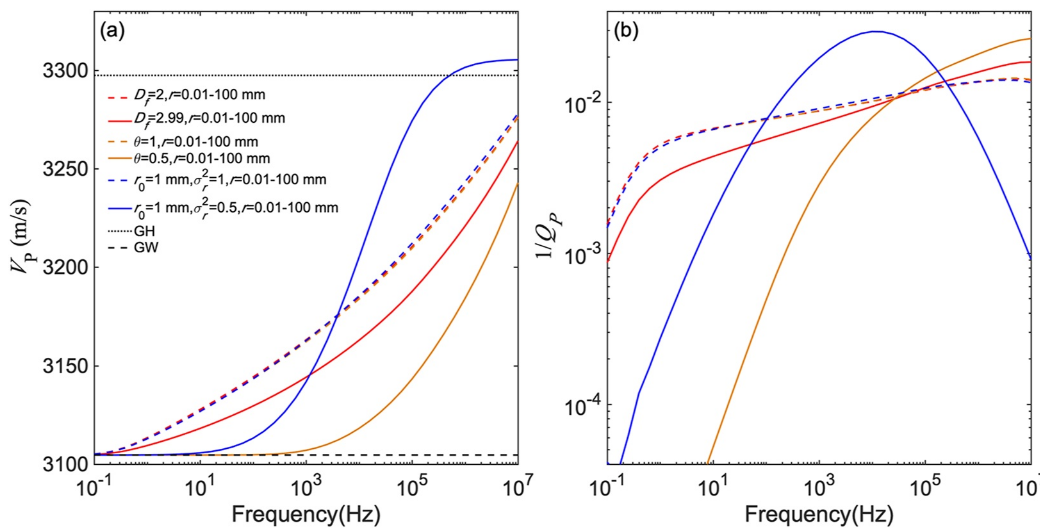

Figure 7. P-wave velocity (a) and attenuation (b) as a function of frequency for self-similar, exponential and Gaussian distributions of the inclusion fluid, where 5% weakly compressible gas is the inclusion fluid.

10.1029/2021JB023809

Table 2
Properties of Limestone and Fluids

Rock		Fluids	
K_b	Varying	K_{fw} (Water)	2.223 GPa
G_b	Varying	ρ_w	997 kg/m^3
K_s	78 GPa	η_w	0.001 Pa•s
ρ_s	2,695.4 kg/m^3	K_{fa} (Air)	0.001011 GPa
ϕ	0.1248	ρ_a	117 kg/m^3
κ	0.1 mD	η_a	0.000015 Pa•s

The experiment consists in drying a sample fully saturated with water in an oven to vary the water saturation. The sample and a standard material specimen are placed in a forced-oscillation device (e.g., Mikhaltsevitch et al., 2021; Spencer, 1981). The description of the experimental setup can be found in Li, Wang, et al. (2020) and Li, Zhao, et al. (2020). A sinusoidal oscillated axial stress excited by piezoelectric transducers (PZTs) is applied to the sample, and the axial and radial amplitudes are measured by using strain gauges, which are glued onto the surfaces of the sample and standard material. Finally, the stress-strain relations of the sample are measured at seismic frequencies (2–500 Hz) and room temperature (~20°C) for different water saturations (0%–87%). During the experiment, the pore and confining pressures are set to 0 MPa, and the vertical stress is maintained at a constant value of 1.4 MPa at all saturations. Because the sample surface is open to the atmosphere and no confining pressure is applied, the sample cannot be maintained in a state of full saturation. However, the open boundary condition should not contribute to the attenuation and dispersion, since the permeability of the sample is low. The properties of the limestone sample and fluids are given in Table 2.

From the measured stress and strain, Young's modulus, extensional attenuation ($1/Q_E$) and Poisson ratio of the limestone sample are determined. Assuming that the sample is homogenous and isotropic, we calculate the bulk (K) and shear (G) moduli at different water saturations (see Figure 8). Regarding the bulk modulus, the measurements are independent of frequency at dry conditions, while they show a clear frequency dependence at partial saturation. As expected, the shear modulus has a much lower frequency dependence than the bulk modulus. We also note that the bulk modulus decreases with increasing saturations in the entire saturation range $S_w = 0\%–87\%$, while the shear modulus decreases in the saturation range $S_w = 0\%–16\%$, then increases at $S_w = 16\%–51\%$ and finally decreases at $S_w = 51\%–87\%$. The effects of pore fluid on the bulk and shear moduli are mechanically different. The compressional-wave-induced fluid flow is the main contributor of the variability in bulk modulus, while both the compressional and shear interactions between the host frame and inclusions may affect shear modulus, which may be highly dependent on the inclusion shape (Quintal et al., 2012). Hence the trends of both moduli are inconsistent.

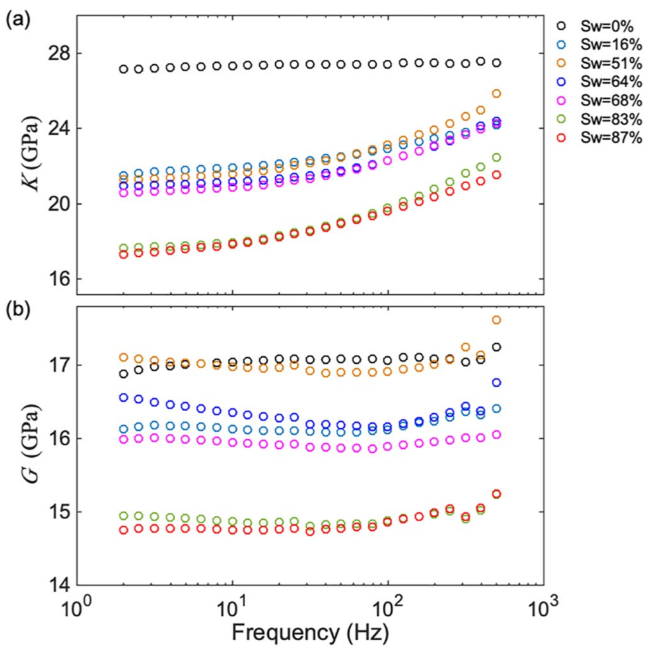

Figure 8. Measured bulk (a) and shear moduli (b) of the limestone sample at zero differential pressure and different water saturations.

As is shown in Figure 8, elastic softening (general decrease of the modulus with increasing saturation) is observed, often thought to be caused by water adsorption at the grain contacts (e.g., Goertz & Knight, 1998; King et al., 2000; Pimienta et al., 2019; Yurikov et al., 2018). Another possible reason for this phenomenon is that the presence of water in limestone causes chemically weakening of the calcite skeleton (e.g., Andreassen & Fabricius, 2010; Risnes et al., 2003). This suggests that the measurements at different water saturations may not be modeled by using the measured dry-rock elastic moduli. This effect cannot be described by the reported theoretical models, and Sun and Gurevich (2020) proposed an approach where effective dry-rock moduli are obtained from measurements at the lowest frequency (where it can be observed that there is almost no dispersion around the left end of the low frequency band in Figure 8 and the sample is assumed to be completely relaxed) by inverting the Gassmann equation. To interpret the laboratory data, we followed the Sun and Gurevich approach and modeled the relative changes of the modulus K with respect to the values measured at the lowest frequency, which are frequency-dependent. The effective dry-rock bulk and shear moduli of limestone are estimated for $S_w = 16\%$, 51%, 64%, 68%, 83%, and 87%, which are 21.71/16.24 GPa, 21.35/17.14 GPa, 20.99/16.56 GPa, 20.63/16.03 GPa, 17.68/14.96 GPa, and 17.37/14.77 GPa, respectively. Compared with the measured dry-rock elastic moduli ($K_b = 27.1$ GPa and $G_b = 16.87$ GPa), we note that the effect of the elastic softening increases with increasing S_w, perhaps because the contact area between water and grains increases with saturation. A similar behavior can be found in the experimental data of Adam et al. (2009).

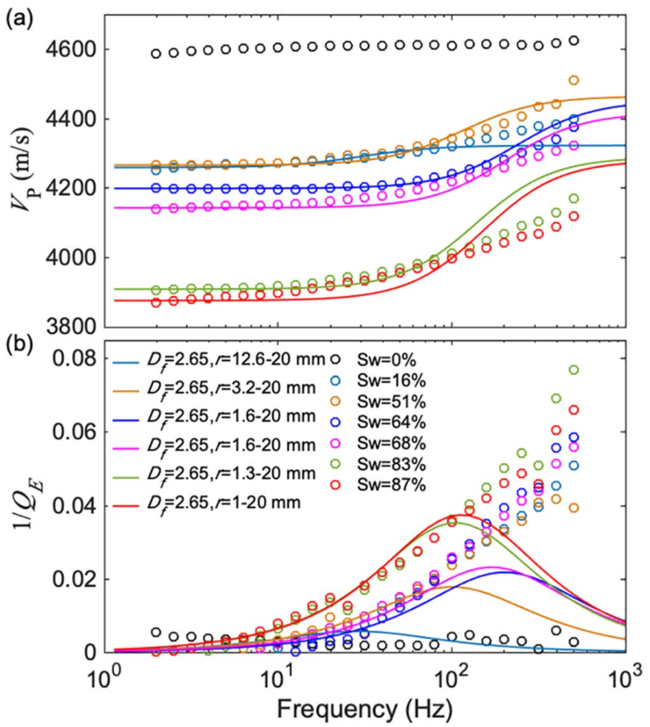

Figure 9. Comparison between the measured P-wave velocity (a) and $1/Q_E$ (b) of the limestone sample at different water saturations (circles) with the modeling results (solid lines), where a self-similar distribution of the fluid patches is assumed.

Figure 9 compares the measurements at different saturations with the modeling results. Considering that the relationship between the fractal dimension D_f and saturation is nonunique for a partially saturated rock (Zhang et al., 2015), we assume that the value of D_f is a constant for the limestone sample, and a fitting parameter which is obtained by a least-square regression on the measurements. Hence, with the corresponding values of $D_f = 2.65$ and $r = 12.6$–20 mm, $D_f = 2.65$ and $r = 3.2$–20 mm, $D_f = 2.65$ and $r = 1.6$–20 mm, $D_f = 2.65$ and $r = 1.6$–20 mm, $D_f = 2.65$ and $r = 1.3$–20 mm and $D_f = 2.65$ and $r = 1$–20 mm, the IPMPS model describes well the measurements. Furthermore, the predicted characteristic frequency shifts to higher frequencies from $S_w = 16\%$ to 64%, and to lower frequencies from $S_w = 64\%$ to 87%.

The discrepancy between the modeled $1/Q_E$ and the measurements is possibly related to the presence of attenuation induced by fabric heterogeneities. Since the theoretical $1/Q_E$ is estimated from the relation $(1-\nu)(1-2\nu)/Q_P = (1+\nu)/Q_E - 2\nu(2-\nu)/Q_S$ (ν is the Poisson ratio of the partially saturated rock), the S-wave attenuation ($1/Q_S$) induced by the WILFF is likely to be present in the rocks (Quintal et al., 2012), while it is not considered into our model. Additionally, the discrepancy can also be attributed to the fact the fluid distribution in the sample does not necessarily correspond to a representative elementary volume (REV). We also note that the motion of the liquid-gas interface is not included into our model. However, vibration of the interface at very high frequencies may dissipate energy, which could also partially explain the discrepancy between the observed and modeled attenuation at very high frequencies. We also observed that when D_f is constant, the scale range decreases with increasing air saturation, indicating that when water in the sample is drained out, the size of the regions occupied by air becomes larger.

Figure 10 shows the comparison as a function of water saturation and four seismic frequencies. It is observed that the measured P-wave velocities are almost constant for S_w less than 51%. This behavior may be related to the location of the strain gauges, that is, when S_w is low, the gauges are placed in regions saturated with air (Li, Zhao, et al., 2020; Pimienta et al., 2017). As S_w further increases to 87%, the measured velocities decrease obviously, and the measured $1/Q_E$ increases with increasing S_w. The theoretical results follow the same trend as those of the measurements.

4.2. Tight Carbonate

In the next example, the IPMPS model is applied to a tight carbonate sample measured by Li, Wang, et al. (2020), whose porosity is 5.34% and permeability is 0.1 mD (a cylinder with 38 mm in diameter and 50 mm in length). The elastic moduli and attenuation are measured at seismic frequencies (1–1000 Hz) and a differential pressure of 19 MPa (the confining and pore pressures are 20 and 1 MPa, respectively) for different water saturations (the saturation was controlled by injecting the volume of the fluid) by using the forced-oscillation method. The properties are given in Table 3.

Figure 11 compares theory and experiment. The dry-rock elastic moduli are estimated from the undrained measurements at the lowest frequency (Sun & Gurevich, 2020), where the inverted dry-rock bulk/shear moduli are 40.22/31.03 GPa, 41.85/31.2 GPa, 43.33/31.38 GPa, 44.68/31.26 GPa, 45.88/31.26 GPa, 47.12/31.38 GPa, 48.48/31.62 GPa, and 50.77/31.65 GPa for $S_w = 20\%$, 30%, 40%, 50%, 60%, 70%, 80%, and 90%, respectively. Compared with the measured dry-rock elastic moduli (38.44/31.68 GPa), the effect of the unrelaxed fluid pressure on the bulk modulus is high, but the effect on the shear modulus can be neglected. This is in contrast to the measurements in the limestone. The tight carbonate sample has low porosity and permeability, and these features may hinder fluid communication between the micropores (related to clay or poorly-connected microcracks/pores) and intergranular pores (Li, Wang, et al., 2020). The water is more likely to be trapped in the micropores as water saturation increases, stiffening the rock skeleton. Hence, the amount of water associated with microporosities

Journal of Geophysical Research: Solid Earth 10.1029/2021JB023809

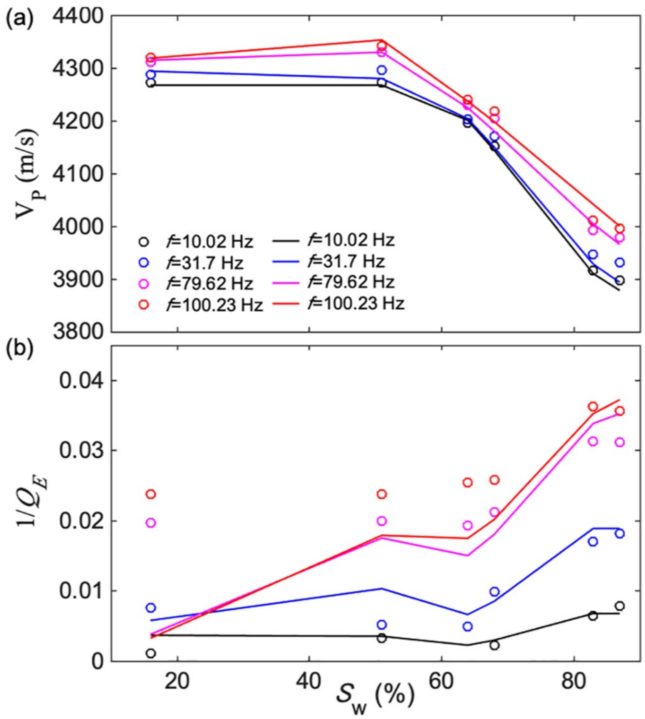

Figure 10. Comparison between the measured P-wave velocity (a) and $1/Q_E$ (b) of the limestone sample (circles) as a function of water saturations and four seismic frequencies with the modeling results (solid lines), where a self-similar distribution of the fluid patches is assumed.

increases, indicating that the dry-rock bulk modulus obtained from the undrained measurements increases with saturation.

Figure 11a shows that the velocity as a function of frequency agrees with the measurements, with values of $D_f = 2.56$ and $r = 12$–15 mm, $D_f = 2.56$ and $r = 4.7$–15 mm, $D_f = 2.56$ and $r = 2.4$–15 mm, $D_f = 2.56$ and $r = 1.5$–15 mm, $D_f = 2.56$ and $r = 0.95$–15 mm, $D_f = 2.56$ and $r = 0.95$–15 mm, $D_f = 2.56$ and $r = 0.75$–15 mm and $D_f = 2.56$ and $r = 0.75$–15 mm for $S_w = 20\%$–90%. We observe similar features as in Figure 9: when D_f is constant, the scale range increases with increasing water saturation. Figure 11b compares results as a function of water saturation and four seismic frequencies. The velocity increases as S_w increases, which differs from that of the limestone sample. Note that the predicted dispersion also increases with increasing S_w.

4.3. Berea Sandstone

The experimental data of a Berea sandstone sample (40 mm in diameter and 80 mm in length) is reported by Chapman et al. (2021), where the frequency dependent P-wave velocity and attenuation are measured between 0.1 and 1000 Hz by using the forced oscillation method. The sample (porosity 19.6% and permeability 270 mD) is dominated by quartz (~80%–95%) and feldspar and clays (3%–8%) (Chapman et al., 2019; Kareem et al., 2017). In the experiments, the dry sample was first flushed with CO_2 to remove the air from the pore space and deionized water was injected to achieve full saturation. Then, water saturated with CO_2 was injected at a fluid pressure greater than 1.2 MPa to replace the deionized water and the distribution of CO_2 in the pore spaces was controlled by reducing the fluid pressure. The properties are given in Table 4.

Figure 12 compares the measurements from experiment Exs-3 with the modeling results. It is observed that when $D_f = 2.78$ and $r = 2$–20 mm, $\theta = 0.04$ and $r = 2$–20 mm, and $r_0 = 6.3$ mm, $\sigma_r^2 = 0.5$, and $r = 2$–20 mm, the measured P-wave velocities are lower than the theoretical ones (Figure 12a). According to Pimienta et al. (2016) and Chapman et al. (2021), the difference between the measured and predicted P-wave velocities at the low frequency end may be due to the presence of CO_2 in the remaining volume of the fluid lines, which results in the sample being partially drained. The present model can provide a reasonable match with the measured P-wave attenuation (Figure 12b). The discrepancy between the observed and modeled attenuation at very high frequencies may be also related to the vibration of the liquid-gas interface, which may dissipate energy. The characteristic frequency in modeling results is around 150 Hz.

Figure 13 compares the measurements from experiment Exs-4 with the modeling results. The theory provides a better match for $D_f = 2.78$ and $r = 1$–20 mm, $\theta = 0.08$ and $r = 1$–20 mm, and $r_0 = 4$ mm, $\sigma_r^2 = 0.8$, and $r = 1$–20 mm. All the rock properties except for the fitting parameters are set according to the theoretical analysis and experimental measurement. These parameters can be obtained on the basis of the thin section, SEM or micro-CT analysis by using an autocorrelation function method (e.g., Krohn, 1988; Toms-Stewart et al., 2009). The characteristic frequency is approximately 500 Hz. Because the pressure decline rate (6.5 MPa/min) in experiment Exs-3 is larger than that of experiment Exs-4 (0.02 MPa/min), the range of inclusion radii (i.e., radii of the gas pockets) from the latter case is slightly wider than that of the former case, which indicates that the range of the inclusions is increased by allowing for smaller inclusions, so that the pressure diffusion is occurring over a shorter length scale which moves the characteristic frequency to higher frequencies. The difference between theory and experiment for attenuation may be related to the additional attenuation in the dry sample, that is, the measured attenuation is the sum of the wave-induced fluid flow one and that of the dry sample

Table 3
Properties of the Tight Carbonate and Fluids (Li, Wang, et al., 2020)

Rock		Fluids	
K_b	Varying	K_{fw} (Water)	2.25 GPa
G_b	Varying	ρ_w	980 kg/m^3
K_s	72 GPa	η_w	0.001 Pa•s
ρ_s	2,870 kg/m^3	K_{fa} (Air)	0.001 GPa
ϕ	0.0534	ρ_a	117 kg/m^3
κ	0.1 mD	η_a	0.000015 Pa•s

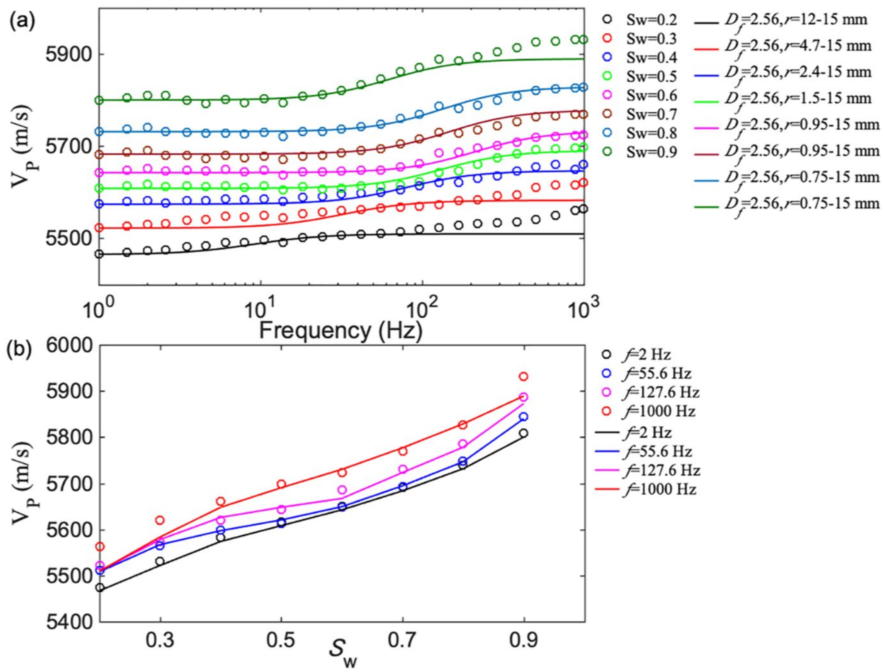

Figure 11. (a) Comparison between the measured P-wave velocity (circles) of the carbonate sample (Li, Wang, et al., 2020) at different water saturations versus frequency (a) and frequencies versus water saturation (b) with the modeling results (solid lines). A self-similar distribution of the fluid patches is assumed.

(Johnston et al., 1979; Kuteynikova et al., 2014; Tisato & Quintal, 2013). Again, the presence of attenuation due to fabric heterogeneities is another reason for the difference.

When the liquid saturations are low, the assumption of dilute inclusions does not hold. Usually, self-consistent versions of the differential effective medium theory are used to model materials containing high concentrations of inclusions (for pure solid composites). However, this approach is not directly applicable to our model, since the double-porosity theory is used to add gas-saturated inclusions into the host material in simulating anelasticity. How to combine the self-consistence and double-porosity theories remains a topic which deserves further work.

5. Conclusions

We present a model for wave propagation in a partially saturated rock, where the fluid patches are characterized by a fractal (self-similar) distribution, and the governing equations are given based on the differential effective medium and Biot-Rayleigh theories. The aim is to model the wave-induced fluid-flow loss of the P waves. The results show that when the inclusions (patches) all have the same size, the P-wave velocity and attenuation are independent of the number of additions, irrespective of the fluid compressibility. The broadband wave-velocity dispersion and attenuation are associated with the fractal dimension D_f and the size of the patches. Comparison with other distributions (exponential and Gaussian) shows that the three distributions provide the same velocities and attenuation for $D_f = 2$, $\theta = 1$ and $\sigma_r^2 = 1$ (when each added inclusion phase has nearly the same volume fraction and inclusion radius), and the range of dispersion and attenuation of $D_f = 2.99/\ \theta = 1/\ \sigma_r^2 = 1$ is wider than that of $D_f < 2.99/\ \theta < 1/\sigma_r^2 < 1$.

To confirm the validity of the model, we have measured the P-wave velocity and extensional attenuation of a partially saturated limestone sample between 2 and 500 Hz at room temperature. The measurements show that the velocity dispersion and attenuation have a broad distribution across that frequency range, while the seismic properties are nearly independent of frequency at

Table 4
Properties of Berea Sandstone and Fluids (Chapman et al., 2021)

Rock		Fluids	
K_b	11.7 GPa	K_{fw} (Water)	2.23 GPa
G_b	11.1 GPa	ρ_w	997.7 kg/m^3
K_s	30 GPa	η_w	0.00091 Pa•s
ρ_s	2,600 kg/m^3	K_{fC} (CO_2)	0.0017 GPa
ϕ	0.196	ρ_C	17.2 kg/m^3
κ	270 mD	η_C	0.000015 Pa•s

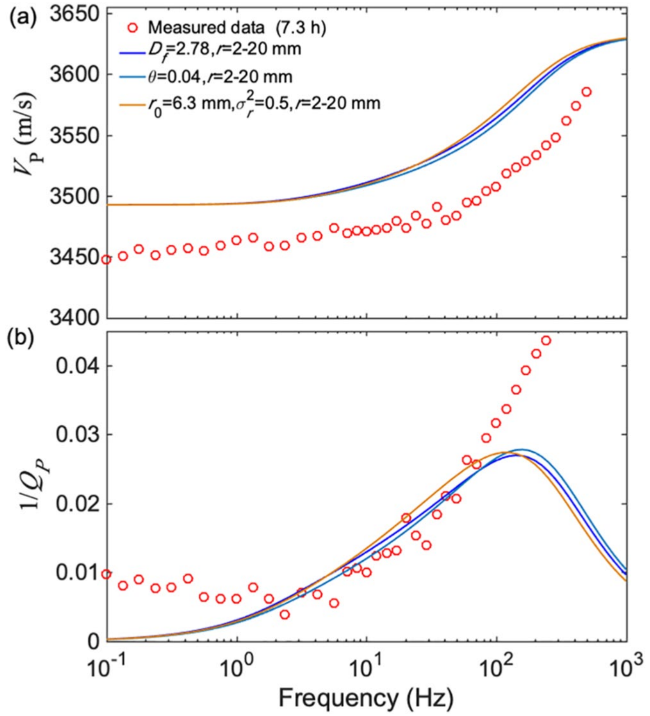

Figure 12. Comparison between the theoretical (solid line) and measured P-wave velocity (a) and attenuation (b) (circles) from experiment Exs-3 (Chapman et al., 2021) at ~0.1% CO_2 saturation (99.9% water) and ~10 MPa differential pressure (7.3 hr is the time spent in the experiment after the initiation of depressurization). The modeling assumes $D_f = 2.78$ and $r = 2$–20 mm, $\theta = 0.04$ and $r = 2$–20 mm, and $r_0 = 6.3$ mm, $\sigma_r^2 = 0.5$, and $r = 2$–20 mm.

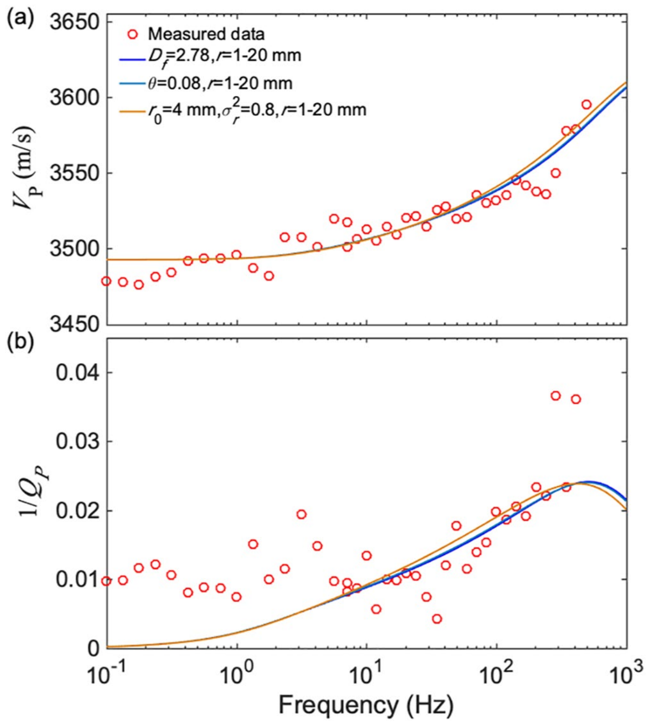

Figure 13. Comparison between the theoretical (solid line) and measured P-wave velocity (a) and attenuation (b) (circles) from experiment Exs-4 (Chapman et al., 2021) at ~0.1% CO_2 saturation (99.9% water) and ~10 MPa differential pressure (6.1 hr is the time spent in the experiment after the initiation of depressurization). The modeling assumes $D_f = 2.78$ and $r = 1$–20 mm, $\theta = 0.08$ and $r = 1$–20 mm, and $r_0 = 4$ mm, $\sigma_r^2 = 0.8$, and $r = 1$–20 mm.

dry conditions. The analysis suggests that the theory provides a reasonable agreement with the measured velocity at different saturations, but is not capable of predicting the attenuation, since the model does not consider the dissipation due to the fabric heterogeneities. Similar results are obtained for a tight carbonate and a sandstone.

Data Availability Statement

The low-frequency measurement data of the limestone sample can be downloaded from the website (https://zenodo.org/record/5515806#.YUb5y54zZTY). The experimental data of tight carbonate and Berea sandstone can be available in Zenodo from https://zenodo.org/record/3707044#.XmmxpW5uKqk (Li, Wang, et al., 2020) and https://doi.org/10.5281/zenodo.4401884 (Chapman et al., 2021).

Acknowledgments
The authors are grateful to Yves Bernabé, the associate editor and anonymous reviewers for their valuable comments. Jing Ba thanks Dr. Q. Yao for his assistance in the low frequency measurements on the limestone specimen during his visit to University of Houston. Jing Ba and Lin Zhang are grateful to Dr. H. Li for helpful discussions. The authors are grateful to the support of the Jiangsu Innovation and Entrepreneurship Plan, Jiangsu Province Science Fund for Distinguished Young Scholars, Natural Science Foundation of Jiangsu Province (BK20210379), and National Natural Science Foundation of China (41974123, 42104110).

References

Adam, L., Batzle, M., Lewallen, K. T., & van Wijk, K. (2009). Seismic wave attenuation in carbonates. *Journal of Geophysical Research: Solid Earth*, *114*(B6). https://doi.org/10.1029/2008JB005890

Agofack, N., Lozovyi, S., & Bauer, A. (2018). Effect of CO_2 on P- and S-wave velocities at seismic and ultrasonic frequencies. *International Journal of Greenhouse Gas Control*, *78*, 388–399. https://doi.org/10.1016/j.ijggc.2018.09.010

Andreassen, K. A., & Fabricius, I. L. (2010). Biot critical frequency applied to description of failure and yield of highly porous chalk with different pore fluids. *Geophysics*, *75*(6), E205–E213. https://doi.org/10.1190/1.3504188

Ba, J., Carcione, J. M., Cao, H., Du, Q. Z., Yuan, Z. Y., & Lu, M. H. (2012). Velocity dispersion and attenuation of P waves in partially-saturated rocks: Wave propagation equations in double-porosity medium. (in Chinese). *Chinese Journal of Geophysics*, *55*(1), 219–231. https://doi.org/10.6038/j.issn.0001-5733.2012.01.021

Ba, J., Carcione, J. M., & Nie, J. X. (2011). Biot-Rayleigh theory of wave propagation in double-porosity media. *Journal of Geophysical Research: Solid Earth*, *116*, B06202. https://doi.org/10.1029/2010JB008185

Ba, J., Ma, R., Carcione, J. M., & Picotti, S. (2019). Ultrasonic wave attenuation dependence on saturation in tight oil siltstones. *Journal of Petroleum Science and Engineering*, *179*, 1114–1122. https://doi.org/10.1016/j.petrol.2019.04.099

Ba, J., Xu, W., Fu, L. Y., Carcione, J. M., & Zhang, L. (2017). Rock anelasticity due to patchy saturation and fabric heterogeneity: A double double-porosity model of wave propagation. *Journal of Geophysical Research: Solid Earth*, *122*(3), 1949–1976. https://doi.org/10.1002/2016JB013882

Berryman, J. G. (1979). Theory of elastic properties of composite materials. *Applied Physics Letters*, *35*(11), 856–858. https://doi.org/10.1063/1.90982

Berryman, J. G. (1992). Single-scattering approximations for coefficients in Biot's equations of poroelasticity. *Journal of the Acoustical Society of America*, *91*(2), 551–571. https://doi.org/10.1121/1.402518

Biot, M. A. (1956). Theory of propagation of elastic waves in a fluid-saturated porous solid. I. Low-frequency range. *Journal of the Acoustical Society of America*, *28*(2), 168–178. https://doi.org/10.1121/1.1908239

Cadoret, T., Marion, D., & Zinszner, B. (1995). Influence of frequency and fluid distribution on elastic wave velocities in partially saturated limestones. *Journal of Geophysical Research: Solid Earth*, *100*(B6), 9789–9803. https://doi.org/10.1029/95jb00757

Cadoret, T., Mavko, G., & Zinszner, B. (1998). Fluid distribution effect on sonic attenuation in partially saturated limestones. *Geophysics*, *63*, 154–160. https://doi.org/10.1190/1.1444308

Carcione, J. M., Helle, H. B., & Pham, N. H. (2003). White's model for wave propagation in partially saturated rocks: Comparison with poroelastic numerical experiments. *Geophysics*, *68*(4), 1389–1398. https://doi.org/10.1190/1.1598132

Carcione, J. M., Santos, J. E., & Picotti, S. (2011). Anisotropic poroelasticity and wave-induced fluid flow: Harmonic finite-element simulations. *Geophysical Journal International*, *186*(3), 1245–1254. https://doi.org/10.1111/j.1365-246X.2011.05101.x

Chapman, S., Borgomano, J. V., Quintal, B., Benson, S. M., & Fortin, J. (2021). Seismic wave attenuation and dispersion due to partial fluid saturation: Direct measurements and numerical simulations based on X-ray CT. *Journal of Geophysical Research: Solid Earth*, *126*(4), e2021JB021643. https://doi.org/10.1029/2021JB021643

Chapman, S., Borgomano, J. V. M., Yin, H., Fortin, J., & Quintal, B. (2019). Forced oscillation measurements of seismic wave attenuation and stiffness moduli dispersion in glycerine-saturated Berea sandstone. *Geophysical Prospecting*, *67*, 956–968. https://doi.org/10.1111/1365-2478.12710

Chapman, S., Quintal, B., Holliger, K., Baumgartner, L., & Tisato, N. (2018). Laboratory measurements of seismic attenuation and Young's modulus dispersion in a partially and fully water-saturated porous sample made of sintered borosilicate glass. *Geophysical Prospecting*, *66*(7), 1384–1401. https://doi.org/10.1111/1365-2478.12643

Ciz, R., Gurevich, B., & Markov, M. (2006). Seismic attenuation due to wave-induced fluid flow in a porous rock with spherical heterogeneities. *Geophysical Journal International*, *165*(3), 957–968. https://doi.org/10.1111/j.1365-246X.2006.02968.x

Dutta, N. C., & Seriff, A. J. (1979). On White's model of attenuation in rocks with partial gas saturation. *Geophysics*, *44*, 1806–1812. https://doi.org/10.1190/1.1440940

Endres, A. L., & Knight, R. (1991). The effects of pore-scale fluid distribution on the physical properties of partially saturated tight sandstones. *Journal of Applied Physics*, *69*(2), 1091–1098. https://doi.org/10.1063/1.347376

Feder, J. (1988). *Fractals*. Plenum.

Gassmann, F. (1951). Uber die Elastizitat poroser medien. *Veirteljahrasschrift der Naturforschen- den Gesellschaft in Zurich*, *96*, 1–23.

Goertz, D., & Knight, R. (1998). Elastic wave velocities during evaporative drying. *Geophysics*, *63*(1), 171–183. https://doi.org/10.1190/1.1444310

Helle, H. B., Pham, N. H., & Carcione, J. M. (2003). Velocity and attenuation in partially saturated rocks: Poroelastic numerical experiments. *Geophysical Prospecting*, *51*(6), 551–566. https://doi.org/10.1046/j.1365-2478.2003.00393.x

Hill, R. (1963). Elastic properties of reinforced solids: Some theoretical principles. *Journal of the Mechanics and Physics of Solids*, *11*, 357–372. https://doi.org/10.1016/0022-5096(63)90036-X

Johnson, D. L. (2001). Theory of frequency dependent acoustics in patchy-saturated porous media. *Journal of the Acoustical Society of America*, *110*(2), 682–694. https://doi.org/10.1121/1.1381021

Johnston, D. H., Toksöz, M. N., & Timur, A. (1979). Attenuation of seismic waves in dry and saturated rocks: II. Mechanisms. *Geophysics*, *44*(4), 691–711. https://doi.org/10.1190/1.1440970

Kareem, R., Cubillas, P., Gluyas, J., Bowen, L., Hillier, S., & Greenwell, H. C. (2017). Multi-technique approach to the petrophysical characterization of Berea sandstone core plugs (Cleveland Quarries, USA). *Journal of Petroleum Science and Engineering*, *149*, 436–455. https://doi.org/10.1016/j.petrol.2016.09.029

King, M. S., Marsden, J. R., & Dennis, J. W. (2000). Biot dispersion for P- and S-wave velocities in partially and fully saturated sandstones. *Geophysical Prospecting*, *48*(6), 1075–1089. https://doi.org/10.1111/j.1365-2478.2000.00221.x

Klimeš, L. (2002). Correlation functions of random media. *Pure and Applied Geophysics*, *159*(7), 1811–1831. https://doi.org/10.1007/s00024-002-8710-2

Kobayashi, Y., & Mavko, G. (2016). Variation in P-wave modulus with frequency and water saturation: Extension of dynamic-equivalent-medium approach. *Geophysics*, *81*(5), D479–D494. https://doi.org/10.1190/geo2015-0045.1

Krohn, C. E. (1988). Sandstone fractal and Euclidean pore volume distributions. *Journal of Geophysical Research: Solid Earth*, *93*(B4), 3286–3296. https://doi.org/10.1029/JB093iB04p03286

Kuteynikova, M., Tisato, N., Jänicke, R., & Quintal, B. (2014). Numerical modeling and laboratory measurements of seismic attenuation in partially saturated rock. *Geophysics*, *79*(2), L13–L20. https://doi.org/10.1190/geo2013-0020.1

Lebedev, M., Pervukhina, M., Mikhaltsevitch, V., Dance, T., Bilenko, O., & Gurevich, B. (2013). An experimental study of acoustic responses on the injection of supercritical CO_2 into sandstones from the Otway Basin. *Geophysics*, *78*(4), D293–D306. https://doi.org/10.1190/geo2012-0528.1

Le Ravalec, M., Guéguen, Y., & Chelidze, T. (1996). Elastic wave velocities in partially saturated rocks: Saturation hysteresis. *Journal of Geophysical Research: Solid Earth*, *101*(B1), 837–844. https://doi.org/10.1029/95JB02879

Li, H., Wang, D., Gao, J., Zhang, M., Wang, Y., Zhao, L., & Yang, Z. (2020). Role of saturation on elastic dispersion and attenuation of tight rocks: An experimental study. *Journal of Geophysical Research: Solid Earth*, *125*(4), e2019JB018513. https://doi.org/10.1029/2019JB018513

Li, H., Zhao, L., Han, D. H., Gao, J., Yuan, H., & Wang, Y. (2020). Experimental study on frequency-dependent elastic properties of weakly consolidated marine sandstone: Effects of partial saturation. *Geophysical Prospecting*, *68*(9), 2808–2824. https://doi.org/10.1111/1365-2478.13031

Lumley, D. E. (2001). Time-lapse seismic reservoir monitoring. *Geophysics*, *66*(1), 50–53. https://doi.org/10.1190/1.1444921

Ma, X. Y., Wang, S. X., Zhao, J. G., Yin, H. J., & Zhao, L. M. (2018). Velocity dispersion and fluid substitution in sandstone under partially saturated conditions. *Applied Geophysics*, *15*(2), 188–196. https://doi.org/10.1007/s11770-018-0683-8

Masson, Y. J., & Pride, S. R. (2007). Poroelastic finite difference modeling of seismic attenuation and dispersion due to mesoscopic-scale heterogeneity. *Journal of Geophysical Research: Solid Earth*, *112*(B3). https://doi.org/10.1029/2006JB004592

Masson, Y. J., & Pride, S. R. (2011). Seismic attenuation due to patchy saturation. *Journal of Geophysical Research: Solid Earth*, *116*(B3). https://doi.org/10.1029/2010JB007983

Mavko, G., & Nolen-Hoeksema, R. (1994). Estimating seismic velocities at ultrasonic frequencies in partially saturated rocks. *Geophysics*, *59*(2), 252–258. https://doi.org/10.1190/1.1443587

Mavko, G., & Nur, A. (1979). Wave attenuation in partially saturated rocks. *Geophysics*, *44*(2), 161–178. https://doi.org/10.1190/1.1440958

Mikhaltsevitch, V., Lebedev, M., Chavez, R., Vargas, E. A., Jr., & Vasquez, G. F. (2021). A laboratory forced-oscillation apparatus for measurements of elastic and anelastic properties of rocks at seismic frequencies. *Frontiers in Earth Science*, *9*, 155. https://doi.org/10.3389/feart.2021.654205

Mikhaltsevitch, V., Lebedev, M., & Gurevich, B. (2016). Laboratory measurements of the effect of fluid saturation on elastic properties of carbonates at seismic frequencies. *Geophysical Prospecting*, *64*(4-Advances in Rock Physics), 799–809. https://doi.org/10.1111/1365-2478.12404

Monachesi, L. B., Wollner, U., & Dvorkin, J. (2020). Effective pore fluid bulk modulus at patchy saturation: An analytic study. *Journal of Geophysical Research: Solid Earth*, *125*(1), e2019JB018267. https://doi.org/10.1029/2019JB018267

Müller, T. M., & Gurevich, B. (2004). One-dimensional random patchy saturation model for velocity and attenuation in porous rocks. *Geophysics*, *69*(5), 1166–1172. https://doi.org/10.1190/1.1801934

Müller, T. M., Gurevich, B., & Lebedev, M. (2010). Seismic wave attenuation and dispersion resulting from wave-induced flow in porous rocks – A review. *Geophysics*, *75*, 75A147–75A164. https://doi.org/10.1190/1.3463417

Müller, T. M., Toms-Stewart, J., & Wenzlau, F. (2008). Velocity-saturation relation for partially saturated rocks with fractal pore fluid distribution. *Geophysical Research Letters*, *35*(9). https://doi.org/10.1029/2007GL033074

Murphy, W. F., III (1982). Effects of partial water saturation on attenuation in Massilon sandstone and Vycor porous glass. *Journal of the Acoustical Society of America*, *71*(6), 1458–1468. https://doi.org/10.1121/1.387843

Murphy, W. F., III (1984). Acoustic measures of partial gas saturation in tight sandstones. *Journal of Geophysical Research: Solid Earth*, *89*(B13), 11549–11559. https://doi.org/10.1029/JB089iB13p11549

Murphy, W. F., III, Winkler, K. W., & Kleinberg, R. L. (1986). Acoustic relaxation in sedimentary rocks: Dependence on grain contacts and fluid saturation. *Geophysics*, *51*(3), 757–766. https://doi.org/10.1190/1.1442128

Papageorgiou, G., & Chapman, M. (2015). Multifluid squirt flow and hysteresis effects on the bulk modulus–water saturation relationship. *Geophysical Journal International*, *203*(2), 814–817. https://doi.org/10.1093/gji/ggv333

Papageorgiou, G., & Chapman, M. (2017). Wave-propagation in rocks saturated by two immiscible fluids. *Geophysical Journal International*, *209*(3), 1761–1767. https://doi.org/10.1093/gji/ggx128

Picotti, S., Carcione, J. M., Germán Rubino, J., & Santos, J. E. (2007). P-wave seismic attenuation by slow-wave diffusion: Numerical experiments in partially saturated rocks. *Geophysics*, *72*(4), N11–N21. https://doi.org/10.1190/1.2740666

Pimienta, L., Borgomano, J. V., Fortin, J., & Guéguen, Y. (2017). Elastic dispersion and attenuation in fully saturated sandstones: Role of mineral content, porosity, and pressures. *Journal of Geophysical Research: Solid Earth*, *122*(12), 9950–9965. https://doi.org/10.1002/2017JB014645

Pimienta, L., Borgomano, J. V. M., Fortin, J., & Guéguen, Y. (2016). Modeling the drained/undrained transition: Effect of the measuring method and the boundary conditions. *Geophysical Prospecting*, *64*, 1098–1111. https://doi.org/10.1111/1365-2478.12390

Pimienta, L., David, C., Sarout, J., Perrot, X., Dautriat, J., & Barnes, C. (2019). Evolution in seismic properties during low and intermediate water saturation: Competing mechanisms during water imbibition? *Geophysical Research Letters*, *46*(9), 4581–4590. https://doi.org/10.1029/2019GL082419

Pride, S. R., Berryman, J. G., & Harris, J. M. (2004). Seismic attenuation due to wave-induced flow. *Journal of Geophysical Research: Solid Earth*, *109*(B1). https://doi.org/10.1029/2003JB002639

Quintal, B., Steeb, H., Frehner, M., & Schmalholz, S. M. (2011). Quasi-static finite element modeling of seismic attenuation and dispersion due to wave-induced fluid flow in poroelastic media. *Journal of Geophysical Research: Solid Earth*, *116*(B1). https://doi.org/10.1029/2010JB007475

Quintal, B., Steeb, H., Frehner, M., Schmalholz, S. M., & Saenger, E. H. (2012). Pore fluid effects on S-wave attenuation caused by wave-induced fluid flow. *Geophysics*, *77*(3), L13–L23. https://doi.org/10.1190/geo2011-0233.1

Reuss, A. (1929). Berechnung der Fliessgrenzen von Mischkristallen auf Grund der Plastizitätsbedingung für Einkristalle. *Zeitschrift für Angewandte Mathematik und Mechanik*, *9*(1), 49–58. https://doi.org/10.1002/zamm.19290090104

10.1029/2021JB023809

Rieu, M., & Perrier, E. (1998). Fractal models of fragmented and aggregated soils. In B. Philippe, P. Jean-Yves, & A. S. Bobby (Eds.), *Fractals in soil science advances in soil science. Fractals in soil science* (pp. 169–202). CRC Press.

Risnes, R., Haghighi, H., Korsnes, R. I., & Natvik, O. (2003). Chalk–fluid interactions with glycol and brines. *Tectonophysics*, *370*(1–4), 213–226. https://doi.org/10.1016/S0040-1951(03)00187-2

Santos, J. E., & Carcione, J. M. (2015). Finite-element harmonic experiments to model fractured induced anisotropy in poroelastic media. *Computer Methods in Applied Mechanics and Engineering*, *283*, 1189–1213. https://doi.org/10.1016/j.cma.2014.08.016

Santos, J. E., Carcione, J. M., & Picotti, S. (2011). Viscoelastic-stiffness tensor of anisotropic media from oscillatory numerical experiments. *Computer Methods in Applied Mechanics and Engineering*, *200*(9–12), 896–904. https://doi.org/10.1016/j.cma.2010.11.008

Solazzi, S. G., Guarracino, L., Rubino, J. G., & Holliger, K. (2019). Saturation hysteresis effects on the seismic signatures of partially saturated heterogeneous porous rocks. *Journal of Geophysical Research: Solid Earth*, *124*(11), 11316–11335. https://doi.org/10.1029/2019JB017726

Solazzi, S. G., Guarracino, L., Rubino, J. G., Müller, T. M., & Holliger, K. (2017). Modeling forced imbibition processes and the associated seismic attenuation in heterogeneous porous rocks. *Journal of Geophysical Research: Solid Earth*, *122*(11), 9031–9049. https://doi.org/10.1002/2017JB014636

Spencer, J. W. (1981). Stress relaxations at low frequencies in fluid saturated rocks: Attenuation and modulus dispersion. *Journal of Geophysical Research: Solid Earth*, *86*(B3), 1803–1812. https://doi.org/10.1029/JB086iB03p01803

Sun, Y., & Gurevich, B. (2020). Modeling the effect of pressure on the moduli dispersion in fluid-saturated rocks. *Journal of Geophysical Research: Solid Earth*, *125*(8), e2019JB019297. https://doi.org/10.1029/2019JB019297

Szewczyk, D., Holt, R. M., & Bauer, A. (2018). The impact of saturation on seismic dispersion in shales—Laboratory measurements. *Geophysics*, *83*(1), MR15–MR34. https://doi.org/10.1190/geo2017-0169.1

Tisato, N., Madonna, C., & Saenger, E. H. (2021). Attenuation of seismic waves in partially saturated Berea sandstone as a function of frequency and confining pressure. *Frontiers in Earth Science*, *9*, 641177. https://doi.org/10.3389/feart.2021.641177

Tisato, N., & Quintal, B. (2013). Measurements of seismic attenuation and transient fluid pressure in partially saturated Berea sandstone: Evidence of fluid flow on the mesoscopic scale. *Geophysical Journal International*, *195*(1), 342–351. https://doi.org/10.1093/gji/ggt259

Toms, J., Müller, T. M., Ciz, R., & Gurevich, B. (2006). Comparative review of theoretical models for elastic wave attenuation and dispersion in partially saturated rocks. *Soil Dynamics and Earthquake Engineering*, *26*(6–7), 548–565. https://doi.org/10.1016/j.soildyn.2006.01.008

Toms, J., Müller, T. M., & Gurevich, B. (2007). Seismic attenuation in porous rocks with random patchy saturation. *Geophysical Prospecting*, *55*(5), 671–678. https://doi.org/10.1111/j.1365-2478.2007.00644.x

Toms-Stewart, J., Müller, T. M., Gurevich, B., & Paterson, L. (2009). Statistical characterization of gas-patch distributions in partially saturated rocks. *Geophysics*, *74*(2), WA51–WA64. https://doi.org/10.1190/1.3073007

Wang, P., Chen, X., Li, X., Cui, Y. A., & Li, J. (2021). Moduli variations in two-phase fluid rocks considering squirt flow and patchy saturation. *Journal of Petroleum Science and Engineering*, *206*, 109041. https://doi.org/10.1016/j.petrol.2021.109041

Wenzlau, F., Altmann, J. B., & Müller, T. M. (2010). Anisotropic dispersion and attenuation due to wave-induced fluid flow: Quasi-static finite element modeling in poroelastic solids. *Journal of Geophysical Research: Solid Earth*, *115*(B7). https://doi.org/10.1029/2009JB006644

White, J. E. (1975). Computed seismic speeds and attenuation in rocks with partial gas saturation. *Geophysics*, *40*, 224–232. https://doi.org/10.1190/1.1440520

White, J. E., Mikhaylova, N. G., & Lyakhovitskiy, F. M. (1975). Low-frequency seismic waves in fluid-saturated layered rocks. *Journal of the Acoustical Society of America*, *57*(S1), S30–S30. https://doi.org/10.1121/1.1995164

Xiong, F., Liu, J., Guo, Z., & Liu, J. (2021). Wave equations of porous media saturated with two immiscible fluids based on the volume averaging method. *Frontiers in Earth Science*, *9*, 618909. https://doi.org/10.3389/feart.2021.618909

Yu, H., Ba, J., Carcione, J., Li, J. S., Tang, G., Zhang, X. Y., et al. (2014). Rock physics modeling of heterogeneous carbonate reservoirs: Porosity estimation and hydrocarbon detection. *Applied Geophysics*, *11*(1), 9–22. https://doi.org/10.1007/s11770-014-0413-9

Yurikov, A., Lebedev, M., Gor, G. Y., & Gurevich, B. (2018). Sorption-induced deformation and elastic weakening of Bentheim sandstone. *Journal of Geophysical Research: Solid Earth*, *123*, 8589–8601. https://doi.org/10.1029/2018JB016003

Zhang, B., Yang, D., Cheng, Y., & Zhang, Y. (2019). A unified poroviscoelastic model with mesoscopic and microscopic heterogeneities. *Science Bulletin*, *64*(17), 1246–1254. https://doi.org/10.1016/j.scib.2019.05.027

Zhang, L., Ba, J., & Carcione, J. M. (2021). Wave propagation in infinituple-porosity media. *Journal of Geophysical Research: Solid Earth*, *126*(4), e2020JB021266. https://doi.org/10.1029/2020JB021266

Zhang, L., Ba, J., Carcione, J. M., & Fu, L. Y. (2020). Differential poroelasticity model for wave dissipation in self-similar rocks. *International Journal of Rock Mechanics and Mining Sciences*, *128*, 104281. https://doi.org/10.1016/j.ijrmms.2020.104281

Zhang, Y., Nishizawa, O., Kiyama, T., & Xue, Z. (2015). Saturation-path dependency of P-wave velocity and attenuation in sandstone saturated with CO_2 and brine revealed by simultaneous measurements of waveforms and X-ray computed tomography images. *Geophysics*, *80*(4), D403–D415. https://doi.org/10.1190/geo2014-0289.1

Zhao, L., Tang, G., Wang, S., Zhao, J., Wang, X., Liu, H., et al. (2019). Laboratory study of oil saturation and oil/water substitution effects on a sandstone's modulus dispersion and attenuation. *Exploration Geophysics*, *50*(3), 324–335. https://doi.org/10.1080/08123985.2019.1610327